Dewetting-mediated pattern formation in nanoparticle assemblies

2011 J. Phys.: Condens. Matter 23 083001

(http://iopscience.iop.org/0953-8984/23/8/083001)

IOP Publishing Journal of Physics: Condensed Matter

J. Phys.: Condens. Matter **23** (2011) 083001 (19pp) doi:10.1088/0953-8984/23/8/083001

TOPICAL REVIEW

Dewetting-mediated pattern formation in nanoparticle assemblies

Andrew Stannard

School of Physics and Astronomy, University of Nottingham, Nottingham NG7 2RD, UK

E-mail: andrew.stannard@nottingham.ac.uk

Received 9 November 2010
Published 3 February 2011
Online at stacks.iop.org/JPhysCM/23/083001

Abstract

The deposition of nanoparticles from solution onto solid substrates is a diverse subfield of current nanoscience research. Complex physical and chemical processes underpin the self-assembly and self-organization of colloidal nanoparticles at two-phase (solid–liquid, liquid–air) interfaces and three-phase (solid–liquid–air) contact lines. This review discusses key recent advances made in the understanding of nonequilibrium dewetting processes of nanoparticle-containing solutions, detailing how such an apparently simple experimental system can give rise to such a strikingly varied palette of two-dimensional self-organized nanoparticle array morphologies. Patterns discussed include worm-like domains, cellular networks, microscale rings, and fractal-like fingering structures. There remain many unresolved issues regarding the role of the solvent dewetting dynamics in assembly processes of this type, with a significant focus on how dewetting can be coerced to produce nanoparticle arrays with desirable characteristics such as long-range order. In addition to these topics, methods developed to control nanofluid dewetting through routes such as confining the geometries of drying solutions, depositing onto pre-patterned heterogeneous substrates, and post-dewetting pattern evolution via local or global manipulation are covered.

(Some figures in this article are in colour only in the electronic version)

Contents

1. Introduction 1
2. Understanding morphologies and pattern formation mechanisms 3
   2.1. Worm-like and cellular morphologies 3
   2.2. Monte Carlo modelling 6
   2.3. Nanoparticle rings 8
   2.4. Nanoparticle fingering 9
3. Controlling pattern formation 11
   3.1. Droplet drying 11
   3.2. Confined drying geometries 13
   3.3. Heterogeneous substrates 15
   3.4. Post-deposition pattern evolution 16
4. Conclusions 17
Acknowledgments 18
References 18

1. Introduction

The creation of long-range order via self-assembly is one of the key objectives of modern nanoscience. Whether the assemblies of interest are surface-bound molecular crystals or nanoparticle superlattices, the aim is the same—understand the intermolecular/interparticle interactions and physical processes that give rise to structures that are observed, and, armed with this knowledge, tailor conditions to give the desired effect (typically an increase in the ordering range). We concern ourselves here with two-dimensional arrays of colloidal nanoparticles, and their assembly as mediated by the dynamics of solvent dewetting. This review details key advances made by a number of groups in understanding and controlling the self-assembly and self-organization of nanoparticles on solid substrates. We differentiate between the terms 'self-assembly' and 'self-organization' by noting that the former describes a process occurring close to equilibrium in which local

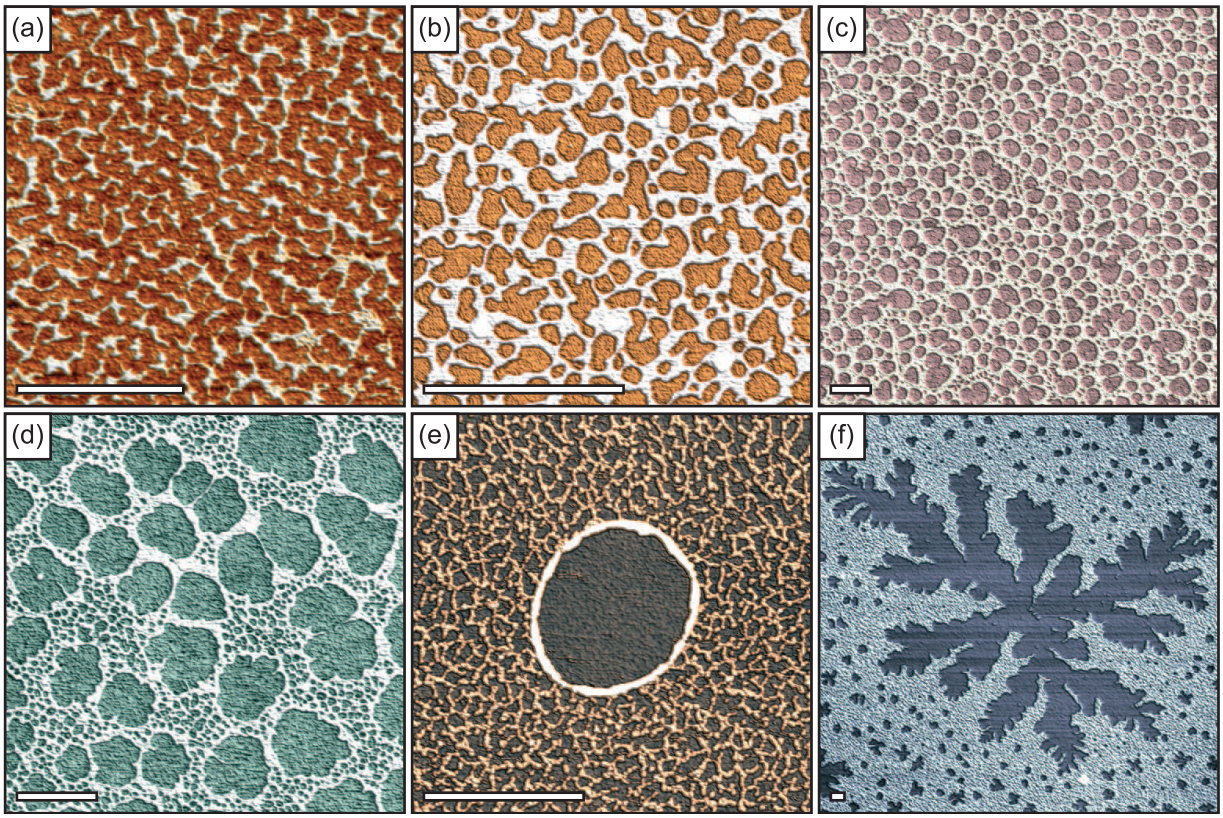

Figure 1. AFM images of various drying-mediated patterns formed by alkanethiol-passivated 2 nm Au nanoparticles on silicon substrates, classified as: (a) worm-like; (b) labyrinthine; (c) a cellular network; (d) a dual-scale cellular network; (e) a microscale ring; and (f) a large viscous-fingering-like structure. Scale bars: 1 μm. The wide range of self-organized morphologies arises due to variations of the nanoparticle concentration, solvent, substrate type, and deposition method.

interactions between component parts drive aggregation, while the latter describes a process occurring far from equilibrium where aggregation of the component parts is driven, and sometimes maintained, by an external factor (such as solvent dewetting). Outcomes of these two processes can usually be distinguished by the characteristic length scale of the resultant structure/pattern. Since self-assembly processes are primarily dictated by interparticle interactions, this is reflected in a periodicity/correlation length approximately corresponding to the size of the component parts. In a self-organization process, correlations typically extend over distances much greater than the interparticle separation. It is self-organized nanoparticle arrays that will concern us here, for the most part, since pattern formation out of equilibrium, not just at the nanoscale, can lead to a wide variety of striking morphologies [1, 2].

The term 'nanofluid' is increasingly being used to describe a suspension of non-volatile nanoparticles (spherical nanoparticles, nanorods, etc) in a volatile organic, or inorganic, solvent. Most attention to dewetting-induced pattern formation has been directed at non-volatile fluids, particularly polymers such as polystyrene [3]. The origin of dewetting in these non-volatile systems are instabilities driven by intermolecular and surface forces. Indeed, Reiter's early work on thin polystyrene films [3] initiated an intense research effort focusing on how the morphology of thin polymer films may be determined by nonequilibrium processes such as nucleation and growth and spinodal dewetting [4]. Furthermore, studies were undertaken to assess how these processes could be controlled, and morphologies predicted, with suitable tailoring of experimental parameters, such as the thickness of the polymer film, and, in the study by Seemann *et al* [5], the thickness of oxide layers on silicon substrates.

When we consider a volatile fluid, the additional possibility of evaporatively driven dewetting opens up the parameter space enormously to give rise to an even richer palette of patterns than would be attainable from instability-driven dewetting alone. Dewetting of volatile nanofluids gives rise to various morphologies as the positions of nanoparticles indicate the history of solvent dewetting moments prior to complete solvent evaporation, which is assumed to arrest the motion of nanoparticles on moderate timescales. A plethora of nonequilibrium self-organized morphologies of nanoparticle arrays have been reported, including isolated islands [6–8], worm-like domains [6, 7], continuous labyrinthine structures and interconnected cellular networks [6, 7, 9–13], rings [9, 13–16], and viscous-fingering-like fractal structures [13, 17]. Figure 1 shows a selection of self-organized nanoparticle arrays, including most of the aforementioned, on silicon substrates. Figures 1(a)–(c) display simple unimodal patterns, whereas figures 1(d)–(f) display more complex patterns with more than one characteristic length scale. The range of morphologies displayed here

arises through the modification of factors such as solute (nanoparticle) concentration, solvent, deposition method, and substrate type (e.g. thickness of oxide layer). One of the main challenges in this field is to understand how nonequilibrium dewetting processes give rise to these patterns, and how they may be controlled. Key steps in understanding the origin of these patterns were taken by Ge and Brus [6] and Rabani *et al* [7], who studied how nucleation and growth and spinodal processes can be evaporatively driven to produce the wide selection of patterns we can observe. These insights are a central focus in the first half of this review.

In many ways, progress in investigating the structure of nanoparticle assemblies goes hand-in-hand with the development of advanced microscopy techniques; without these methods many of the patterns to be discussed here would remain hidden in plain sight. Whilst optical microscopy is still an invaluable tool, its diffraction-limited nature prevents the imaging of intricate nanoparticle superstructures with the required lateral spatial resolution. However, optical methods are still useful for key microscale observations, as demonstrated by Bigioni *et al* [18] by observing the formation of nanoparticle superlattices at the liquid–air interface, and specialized contrast-enhanced techniques can give nanometre vertical resolution to monitor real time development of microscale submonolayer nanopatterns, as shown by Pauliac-Vaujour *et al* [17].

Very frequently, electron microscopy—most commonly transmission electron microscopy (TEM)—is used to image nanoparticle assemblies. Indeed, key early observations of superlattices by Andres *et al* [19] and nanoparticle rings by Ohara *et al* [14] were achieved using TEM, and it remains the tool of choice for many, primarily because its excellent spatial resolution permits the investigation of close-packing in real space, and it can even probe the substructure of individual nanoparticles, as shown, for example, by Carbone *et al* [20] for CdSe/CdS core–shell hybrid nanorods. TEM can also be used to locally modify samples, the electron beam can be used to cross-link thiolated nanoparticles [21]. However, despite the clear benefits of TEM, the choice of substrate, a key component in determining the dewetting nature of a nanofluid, is severely limited, restricting parts of the experimental parameter space of dewetting nanofluids, and hence limiting the range of observable patterns.

Scanning probe microscopy (SPM) techniques provide a different perspective on real space imaging. Whilst scanning tunnelling microscopy (STM) is capable of high resolution imaging of nanoparticles [22], the necessity for electrical conduction places restrictions on the nanoparticles and the substrates used. Atomic force microscopy (AFM), then, provides perhaps the most versatile and balanced technique. AFM places no restrictions on the material properties of the substrate (other than being flat) or of the nanoparticle type, allowing greater probing of the parameter space of nanofluids on solid substrates, imaging reliably from sub-100 nm up to 100 μm—typically the length scale realm of nanofluid dewetting patterns. Of course, depending on the diameter of the nanoparticles in question, individual nanoparticle resolution can be achieved with AFM, as shown, for example, by Tang *et al* with 12 nm PbSe particles [23] and later by Constantinides *et al* with 6 nm Au particles [24]. AFM also provides quantitative height information, and, thus, can be particularly useful for multilayer features. In addition, AFM may be used for the manipulation of nanoparticles, either individually or *en masse* [8]. In addition to real space microscopy techniques, reciprocal space techniques, such as grazing incidence small angle x-ray scattering (GISAXS), allow precise measurements of close-packing, and permit real time observation of global assembly modifications brought about, for example, by thermal annealing, as in the study by Robel *et al* [25].

In recent years, the properties of two- and three-dimensional nanoparticle assemblies have been the subject of intense investigation due to their tunable, programmable nature and their potential use as unique optical and/or electrical materials [26]. However, for this potential to be achieved, reliable and simple methods of creating long-range order must be achieved, as is evident from studies of the electrical properties of self-assembled and self-organized nanoparticle arrays [27–31], where even minor irregularities give wholly different behaviour. Achieving long-range order is no simple task, but control over solvent dewetting is proving to be a viable option for two-dimensional nanoparticle assemblies. Part of this control lies in understanding and tailoring what is occurring at the boundaries between different media, such as liquid–air interfaces [18] or solid–liquid–air contact lines [32].

2. Understanding morphologies and pattern formation mechanisms

We start by looking at some relatively simple patterns—those with a single well-defined characteristic length scale—and discuss a range of different plausible formation mechanisms. This leads into discussion of a Monte Carlo model which underlines the key role of evaporation in pattern formation processes of dewetting nanofluids. With an understanding of how simple patterns may form, we go on to discuss more complex patterns (nanoparticle rings and fingering) and how they can be explained within the framework that has been constructed.

2.1. Worm-like and cellular morphologies

One of the earliest insights into drying-mediated nanoparticle self-organization was provided by Ge and Brus [6]. They proposed that the self-organized worm-like patterns they observed when depositing 4 nm CdSe nanoparticles from chloroform onto highly oriented pyrolytic graphite (HOPG) originate from a fluid–fluid spinodal phase separation (this type of pattern is by no means specific to their particular experimental system; figure 2(a) shows a similar morphology for 2 nm colloidal Au nanoparticles on a silicon substrate). They based their arguments around the phase diagram of a two-dimensional system of particles interacting via a Lennard-Jones potential, as developed by Koch *et al* [33] (see figure 2(b)). This model's application to a drying nanofluid lies in the evaporation of solvent corresponding to a temperature

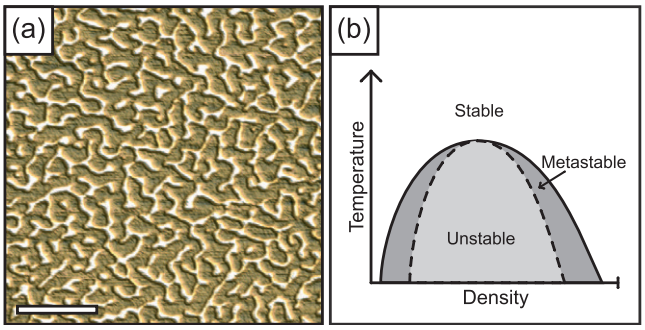

Figure 2. (a) An AFM image of worm-like patterning formed via a spinodal process when spin-coating octanethiol-passivated 2 nm Au nanoparticles dispersed in toluene onto a silicon substrate. Scale bar: 500 nm. (b) Illustrative temperature–density phase diagram of a two-dimensional system of particles interacting via a Lennard-Jones potential, after Koch *et al* [33]. The worm-like structure may be rationalized as a system temperature quench from the stable to unstable region brought about by solvent evaporation.

quench from the coexistence (stable) region to phase separation in the metastable or unstable regions via nucleation and growth or a spinodal process, respectively [6]. This phase transition is driven by a reduction in the screening of interparticle van der Waals interactions via the loss of solvent, and thus gives rise to a range of spatially correlated patterns. Although this model captures key elements of self-organization (large scale correlations from local interactions), the role of solvent fluctuations is ignored; a point that would be addressed by Rabani *et al* [7].

Another common type of self-organized morphology has led to (at least) two competing schools of thought as to how the structure forms. This morphology is a cellular network, a construction that can be thought of as a tessellation of irregular polygons (see figures 1(c) and 3(a)). One way to explain the formation of these structures for a drying nanofluid involves consideration of the hydrodynamic process known as Bénard–Marangoni convection. This is a surface-tension-driven process which can lead to the establishment of convective motion in a polygonal pattern when surface tension inhomogeneities are minimized via flow from warmer to cooler regions. As a result, the surface of a liquid film becomes 'pinched' at the cooler points, which define the outline of the cellular structure. Under certain conditions, Bénard–Marangoni convection gives rise to patterns with a characteristic length scale determined by the film thickness, h, and a dimensionless constant known as the Marangoni number, M_a, given by

$$M_a = \frac{B\Delta T h}{\rho \nu \kappa}, \tag{1}$$

where B is the surface tension gradient ($=-\mathrm{d}\gamma/\mathrm{d}T$), ΔT is the temperature gradient across the liquid film, ρ is the liquid density, ν is the dynamic viscosity, and κ is the thermal diffusivity. This number is a measure of the competing influences of surface tension gradients which act to destabilize the film, and thermal diffusivity and dynamic viscosity which act to nullify film instabilities. For low values of M_a, thermal (and thus surface tension) gradients are neutralized. However, above a critical Marangoni number, $M_c = 80$, convection is present with a well-defined characteristic wavelength, $\lambda = \pi h\sqrt{32/M_a}$. This process establishes convective cells in an irregular polygonal arrangement resulting in the transport of nanoparticles to the convection cell boundaries (cooler regions), thus determining their final positions as the solvent film evaporates globally to produce a cellular network. One should note the subtle difference between Bénard–Marangoni and Rayleigh–Bénard convection [34]. In the former process, it is the free liquid surface and the subsequent surface tension effects which dictate the pattern formation process. The latter process describes a situation where a temperature gradient existing between the upper and lower interfaces of a liquid film establishes convective rolls when a critical Rayleigh number is exceeded. In this case, buoyancy variations are responsible for the emergence of patterning. Silicone oil in a Petri dish heated from beneath is another example of Bénard–Marangoni convection, as demonstrated by Cross and Hohenberg [1]—the critical Marangoni number is exceeded before the critical Rayleigh number (a general result for thin films).

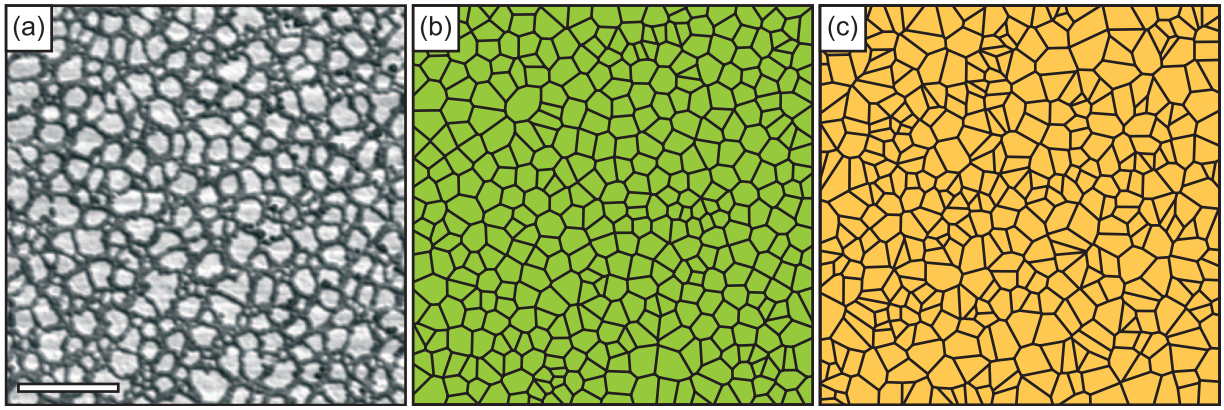

Figure 3. (a) An AFM image of a cellular network formed by spin-coating octanethiol-passivated 2 nm Au nanoparticles dispersed in toluene onto a silicon substrate. Scale bar: 500 nm. (b) The Voronoi tessellation of (a). Analysing the probability distribution of cells having n sides, p_n, gives an entropy value of $S = -\sum_n p_n \ln p_n = 1.48$ and variance of $\mu_2 = \sum_n p_n(n - \langle n\rangle)^2 = 1.19$. (c) The Voronoi tessellation of a completely random Poisson distribution of points, $S = 1.71$ and $\mu_2 = 1.78$. Values of entropy and variance are significantly lower for the nanoparticle network due to its correlated nature.

Maillard *et al* [9, 35] proposed that when a nanoparticle solution is deposited onto a substrate, evaporation of the solvent establishes a temperature gradient across the liquid–air interface. The more volatile the solvent, the greater the temperature gradient, and therefore the greater the value of M_a. It was also suggested that higher concentrations of nanoparticles in solution can increase M_a [35]. Maillard *et al* presented cellular (honeycomb) networks, formed by silver nanoparticles deposited from hexane, which can be attributed to Bénard–Marangoni convection [9, 35]. Subsequently, Stowell and Korgel performed a thorough study of honeycomb networks of gold nanoparticles [10]. They also found that the concentration of nanoparticles in solution plays a large role in determining Marangoni-convection-driven cellular networks. In particular, they examined how this concentration affects the thermal conductivity and surface tension gradient of the thin film. They concluded that dilute solutions are more susceptible to establishing Marangoni convection. However, this leads to experimental difficulties in observing the resultant patterns (frozen-in via global solvent evaporation) as low concentrations of nanoparticles result in poorly defined structures. Therefore, this suggests that there is a narrow parameter range in which Marangoni-convection-driven self-organized nanoparticle networks can be observed experimentally [10]. Despite this clause, Marangoni convection does provide a plausible explanation for the significant spatial correlations that are evident in a wide range of cellular morphologies.

However, it has been shown that Marangoni convection is not the only mechanism through which these types of cellular structure can form. An alternative perspective described by Moriarty *et al* [11] is based on nucleation of a volatile thin film, an idea originating from work on nanoparticle rings by Ohara *et al* [14] (discussed later). If a hole is nucleated in a thin nanofluid film to form a rim (substrate–solvent–air contact line), evaporation of solvent from edge of the rim causes its subsequently expansion. This results in the accumulation of nanoparticles at the contact line which in turn get deposited on the substrate when global evaporation induces complete solvent removal [36] 'freezing' nanoparticles at their current positions. As such, solvent fluctuations may nucleate holes in a nanofluid thin film at random positions. Expanding holes then carry nanoparticles which in turn produce a polygonal network via collision. However, despite the random nucleation positions, the resulting structures possess characteristic spatial correlations due to the coalescence process [11, 12].

To describe these structures quantitatively, rather than just qualitatively, requires the use of various image analysis techniques. Fourier transforms, Voronoi tessellations, and Minkowski morphometry [37] are all excellent image analysis tools to provide quantitative information on self-organized nanoparticle assemblies. Voronoi tessellations, in particular, provide a useful way to extract information from a cellular network image. In this analysis technique the centroid of each cell of a network morphology is found and perpendicular bisectors are drawn for the lines which connect nearest neighbours. For a given centroid point, this technique defines a space which is closer to that point than any other. The plane is filled with cells so that the image is deconstructed into a tessellation of irregular polygons. Figure 3(a) shows a nanoparticle cellular network, and figure 3(b) shows the corresponding Voronoi tessellation.

A key characteristic of a Voronoi tessellation is the probability of finding a cell with n sides, p_n; exploring this probability distribution can reveal order within a structure. Two key parameters which can be extracted from this distribution are the entropy, $S = -\sum_n p_n \ln p_n$, and variance (second central moment), $\mu_2 = \sum_n p_n(n - \langle n \rangle)^2$. S and μ_2 obtained from an experimental cellular network can be compared to those obtained from a Voronoi tessellation of a completely random Poisson set of points (see figure 3(c)) where $S = 1.71$ and $\mu_2 = 1.78$. A network which has lower values of S and μ_2 than those for a random distribution is associated with some degree of order (the expectation value for the mean number of sides is $\langle n \rangle = 6$ for any Voronoi tessellation, irrespective of the extent of order/disorder). It has been shown that colloidal gold nanoparticle networks are spatially correlated [11, 12]: both S and μ_2 are found to be significantly lower than the values expected for a random distribution. Analysis of the experimental network shown in figure 3(a) gives $S = 1.48$ and $\mu_2 = 1.19$. Indeed, visually, one can appreciate the difference between a correlated (figure 3(b)) and random (figure 3(c)) Voronoi tessellation, with the former appearing more ordered. Whilst providing clues towards formation mechanisms, this correlated nature of disorder present in self-organized nanoparticle cellular networks is also of particular importance to their charge transport properties [28, 30, 31].

These random cellular networks represent a recurring pattern in nature that can be found in a variety of two- and three-dimensional physical systems at a range of length scales [38]. Examples of such systems include biological tissues, the hides of giraffes, geological phenomena (e.g. cracked earth, Giant's Causeway (County Antrim, Northern Ireland)), metallurgical grains, and froths and foams. Concerning us here, due to their crystallographic statistical indistinguishability one cannot be sure that a given nanoparticle cellular network has formed through a nucleation and growth process as opposed to Bénard–Marangoni convection, but it is believed to be the process at play for the majority of experimentally observed cellular morphologies since Bénard–Marangoni convection only occurs within a narrow window of parameter space. Since these pattern formation mechanisms are primarily determined by properties of the solvent and the local environment, the resultant pattern morphologies can be observed for a range of solutes, including, for example, organometallic clusters [39] and collagen [40].

A final point of note in this section is the work of Pauliac-Vaujour and Moriarty [41]. Here, a technique was developed to controllably vary the solvent evaporation rate at various positions on the same substrate. This was achieved by depositing a nanofluid solution within a Teflon ring placed on a silicon substrate. Since the solution preferentially wets the Teflon, a meniscus forms and evaporation commences in the centre of the sample where the nanofluid film is thinnest. Due to the shape of the meniscus, the solvent film is thicker at

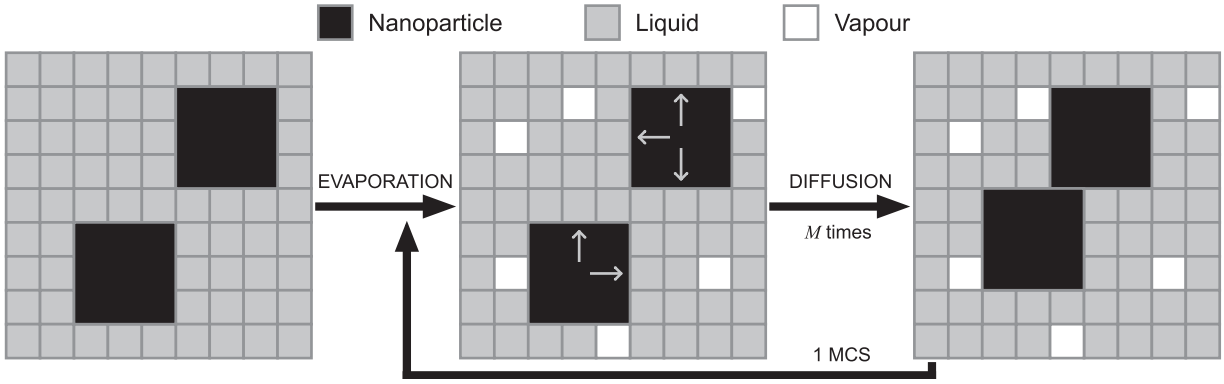

Figure 4. Diagram illustrating the two-dimensional lattice and algorithm used in the model developed by Rabani *et al* [7]. An evaporation cycle is performed, then each nanoparticle is inspected M times; this completes one Monte Carlo sweep. Viable nanoparticle diffusion directions are determined by the liquid coverage of the lattice; nanoparticles may only move in a direction with three adjacent liquid cells.

larger radii, and therefore the evaporation rate is slower. In this way, a transition between the limits of fast and slow solvent evaporation can be observed from the centre of the sample moving outwards. At the centre, where evaporation is most rapid, worm-like patterns are observed (much like that shown in figure 2(a)), indicative of a rapid, spinodal-like formation process. However, moving out from the centre the evaporation rate decreases and cellular network structures (much like the one shown in figure 3(a)) are observed. As such, the results of Pauliac-Vaujour and Moriarty strongly indicate that the rate of solvent evaporation is a key factor in determining pattern formation in drying nanofluids. With this in mind, we move on to discuss a numerical simulation model that is based on solvent fluctuations.

2.2. Monte Carlo modelling

Following on from the work of Ge and Brus [6], Rabani *et al* devised a Monte Carlo model to simulate the drying-mediated two-dimensional assembly of nanoparticles in the presence of solvent fluctuations [7]. This relatively simple model can reproduce an astonishing range of morphologies via the modification of a few simple parameters. Since its inception, many variants on this model have been developed to study more complex situations such as binary mixtures of nanoparticles [42, 43], bimodal patterns [13], patterned substrates [43–45], and three-dimensional behaviour [46, 47]. We will begin by explaining the lattice, algorithm, and Hamiltonian used in the model of Rabani *et al* [7]. This leads into discussion of the system behaviour at different regions of parameter space, the corresponding evaporatively driven dewetting mechanisms, and the resultant pattern morphologies.

Although slightly complicated by the inclusion of nanoparticles, the simulation model of Rabani *et al* is essentially a modification of a simple two-dimensional lattice gas. Each cell of a square lattice, i, with side length, L, is occupied by either solvent, in the liquid ($l_i = 1$) or vapour ($l_i = 0$) phase, or by a nanoparticle ($n_i = 1$); the presence of a nanoparticle excludes the presence of solvent and vice versa. As such, l_i and n_i are binary variables representing the presence (1) or absence (0) of liquid and nanoparticle, respectively, at lattice position i. Periodic boundary conditions apply to the lattice. Solvent occupies single cells of the lattice whereas nanoparticles occupy 3×3 cells, as shown in figure 4. This choice of sizes corresponds to a solvent correlation length of $\xi \approx 1$ nm [7] and 3 nm diameter nanoparticles. (It has been shown, however, that behaviour of this model is largely independent of the relative size of nanoparticles—1×1 size particles give essentially the same results [48].) The initial configuration of the lattice is a predefined concentration of nanoparticles randomly positioned with all other lattice sites occupied by liquid, mimicking a wetting ultrathin nanofluid film (ϕ represents the fraction of the lattice occupied by nanoparticles).

The competing processes of solvent evaporation and nanoparticle diffusion are considered in turn. First, each solvent cell is examined and an attempt is made to convert the solvent phase from liquid to vapour (or vice versa) with a Metropolis acceptance rate $\min[1, \mathrm{e}^{-\Delta E/k_\mathrm{B}T}]$, where ΔE is the change in energy associated with such a move and T is the temperature of the heat bath the system is coupled to. After each solvent cell has been examined, each nanoparticle is examined and an attempt to move it by one lattice spacing in a horizontal or vertical direction is undertaken, again with a Metropolis acceptance rate. Nanoparticles may only move into wet areas of the lattice, that is, in a direction currently occupied by three adjacent liquid cells (see figure 4); this imitates low nanoparticle mobility on a substrate in the absence of liquid solvent [49]. If the nanoparticle moves, the displaced liquid cells are positioned in the nanoparticle's wake to preserve solvent density. To gain control over the rate of nanoparticle diffusion relative to solvent evaporation, each nanoparticle is examined a number of times, given by the mobility ratio, M, per solvent cycle (M can be considered analogous to a nanoparticle diffusion coefficient D [7]). A single Monte Carlo sweep (MCS) is defined as one solvent cycle followed by M nanoparticle cycles. Figure 4 shows the lattice setup for these simulations, and depicts the evaporation–diffusion cycle algorithm.

The Hamiltonian used these simulations may be written as

$$E = -\frac{\epsilon_\mathrm{l}}{2}\sum_{\langle ij\rangle} l_i l_j - \frac{\epsilon_\mathrm{n}}{2}\sum_{\langle ij\rangle} n_i n_j - \frac{\epsilon_\mathrm{nl}}{2}\sum_{\langle ij\rangle} n_i l_j - \mu\sum_i l_i, \quad (2)$$

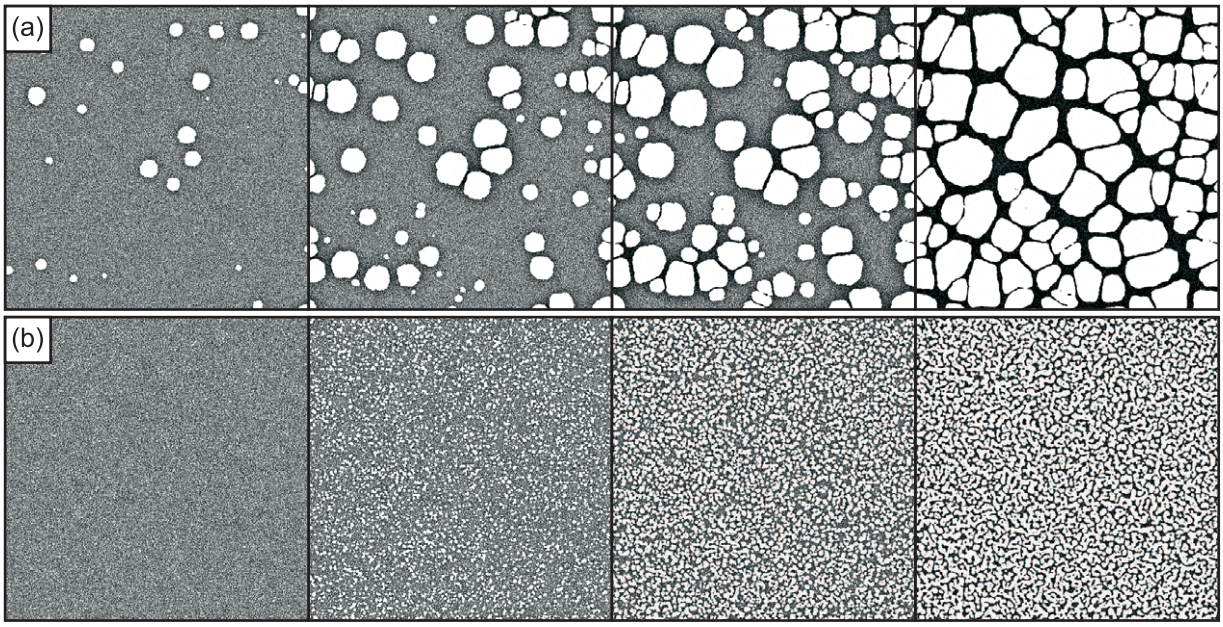

Figure 5. Snapshots of the lattice during two simulations at different temperatures. (a) At the lower temperature, $k_BT = 0.30$, nucleation and growth is observed, leading to a cellular network structure. (b) Increasing the temperature to $k_BT = 0.45$ increases the rate of solvent evaporation and spinodal dewetting is observed. In this case, the spinodal process is approximately one order of magnitude more rapid than the nucleation and growth process. (Simulation parameters: $\mu = -2.30$, $\phi = 0.25$, $M = 30$, $L = 2048$.)

where ϵ_l, ϵ_n, and ϵ_{nl} are the energies of liquid–liquid, nanoparticle–nanoparticle, and nanoparticle–liquid interactions, respectively, μ is the chemical potential, and sums are performed over every site of the lattice. The interactions between lattice cells are limited to nearest- and next-nearest-neighbours, which are given weightings of 1 and $1/\sqrt{2}$, respectively, reflecting a linear decay in interaction strength with distance [12] (initially Rabani *et al* used only nearest-neighbour interactions, resulting in a square-like nature of the patterns they observed [7]). To simplify the parameter space in this model, and to ensure that nanoparticles are well solvated by the liquid prior to solvent evaporation, Rabani *et al* [7] and others [12, 13, 44] fix $\epsilon_n = 2\epsilon_l$ and $\epsilon_{nl} = 1.5\epsilon_l$, at set $\epsilon_l = 1$ to allow all energies to be expressed relative to ϵ_l, leaving k_BT and μ as the only two independent energy scales. (It is worth noting that not all studies of this model have these simplifications in place, Vancea *et al* [48] probe the effect of changing ϵ_{nl} and ϵ_n.)

As a simulation of this model progresses, the liquid phase of the solvent is gradually converted to its equilibrium density; the chemical potential plays the major role in determining this value and the rate of conversion. In a classic lattice gas model, $\mu = -2$ defines the binodal line where both solvent phases are equally favourable. When $\mu < -2$, the vapour phase is energetically more favourable (for low nanoparticle concentrations the binodal line argument holds to a good approximation [48]). Thus, liquid is converted to vapour, and commencing the simulation corresponds to a quench from $\mu = \infty$. When using a sufficiently high mobility ratio, nanoparticles are able to diffuse away from retreating liquid fronts to remain solvated and essentially map the history of dewetting prior to complete solvent evaporation. It should be noted that reference to 'complete solvent evaporation' does not include the evaporation of liquid that may remain as a stable wetting layer around nanoparticles due to the nanoparticle–liquid interaction term. Certain simulation parameters favour a wetting layer which promotes coarsening of nanoparticle assemblies after the initial evaporation stage. Therefore, there are two temporal regimes associated with these simulations—an evaporation stage and a coarsening stage. For now we will concern ourselves with results after the former temporal regime only.

The solvent dewetting mechanism is primarily determined by the parameters μ and T, and so exploration of the associated parameter space is key to understanding this model; approaches have been put forward to efficiently explore the space using genetic algorithms [50]. Nucleation and growth occurs when the rate of liquid-to-vapour conversion is low enough such that only a few random positions in the solvent film are able to nucleate and grow beyond some critical size at which further growth is energetically favourable. In this region of parameter space, the initial liquid layer is in a metastable state; small local fluctuations in solvent density can be recovered, but large enough fluctuations nucleate holes in the film. The resulting morphology is a cellular network which forms via the growth of holes in the ultrathin film. These holes can either coalesce, create a compact region of nanoparticles that form the network branches, or form network nodes at the junction of three of more holes. Figure 5(a) shows an example of nucleation and growth leading to a cellular network.

Despite the random positions of the initial nucleation sites, the final structure possesses correlations due to the growth process through which it forms. This was shown by Martin *et al* [12] by employing the Voronoi tessellation

analysis technique used previously by Moriarty *et al* [11] on colloidal Au nanoparticle networks. Cellular networks from this simulation model display identical behaviour to those observed experimentally, that is, lower values of S and μ_2 compared to a two-dimensional Poisson distribution of points. This gives an element of quantitative agreement between experiment and simulation via statistical crystallography [12].

As the temperature (chemical potential) is increased (decreased), nucleation becomes more frequent, resulting in morphologies where the characteristic length scale decreases. The system is still metastable and dewetting is nucleation and growth dominated, but smaller local fluctuations are required to nucleate holes. Further increasing either of these parameters results in dewetting across the entire liquid–nanoparticle film commencing within a very short time window—a signature of spinodal dewetting. This mechanism produces morphologies formed with a typical length scale—a spinodal wavelength. In this regime, the liquid–nanoparticle film rapidly progresses toward the solvent equilibrium density. Figure 5(b) shows an example of a spinodal process leading to a worm-like/labyrinthine pattern, achieved by an increase in temperature.

The two dewetting mechanisms displayed in figure 5 occur for different simulation parameters, and the temperature dependent spinodal line, $\mu_{sp}(T)$, roughly corresponds to the boundary between the nucleation and growth dominated and spinodal dominated regimes [7, 13]. At this point we recall the results of Pauliac-Vaujour and Moriarty [41] discussed in section 2.1. The results of their experiments and this model are in terrific agreement—a transition from spinodal-like to nucleation and growth patterning may be observed simply from an increase in the rate of solvent evaporation. Thus, this model beautifully displays the role of evaporatively driven dewetting in dictating the patterns formed by drying nanofluids.

A final morphology of note in this section is that of isolated islands of nanoparticles, many examples of which exist in the literature [6–8]. The Monte Carlo model discussed above is capable of forming isolated islands via evaporatively driven dewetting in either an unstable (spinodal) or metastable (nucleation and growth) region of parameter space. In the latter regime, islands may form when the concentration of nanoparticles is low. When this is the case, nucleation and growth of vapour holes drives nanoparticles to aggregate at the nodes of a cellular network structure, with branches ill defined, thus producing an assembly of isolated islands [13] (somewhat analogous behaviour can be seen in the dewetting of polymer films, where cellular structures formed via nucleation and growth decompose into droplets, as observed by Reiter [3]). Issues like this one highlight the difficulty in understanding the exact dewetting mechanism that gives rise to a certain pattern when the only information we have to analyse is the final pattern.

Exhaustive probing of both the μ–T and T–ϕ parameter space can be found elsewhere [13]. Rabani *et al* [7], Martin *et al* [12], Siepmann *et al* [50], and Stannard *et al* [13] all display examples of this model creating morphologies with wonderful visual agreement with experimental images, capturing even the most subtle nuances.

2.3. Nanoparticle rings

We now move on to discuss nanoparticle rings; a pattern typically regarded as a bimodal morphology since rings are generally observed amidst smaller scale patterning (e.g. figure 1(e)). The two patterning types coexisting on the substrate are the remnants of two sequential dewetting processes. The typical mechanisms which result in the small scale patterning have been discussed already and so we turn our attention to the possible mechanisms for the nucleation, growth, and arrest of nanoparticle rings.

Nanofluid dewetting offers a significant number of alternative pathways towards the generation of rings of nanoparticles and nanorods on solid substrates. Many groups have reported the formation of nanoparticle rings, with diameters ranging from a few hundred nm to a few micrometres, composed of, for example, Ag [14], Au [13, 16], Ni [51], FePt [52], and polypyrrole [53] nanoparticles. Due to the complex physical and chemical processes involved in nanofluid dewetting, a wide variety of mechanisms have been put forward to explain the formation of rings of nanoparticles following solvent evaporation. These include nucleation and expansion of holes in the solvent film [10, 13, 36, 47, 54], breath figure formation [55, 56], the Marangoni effect [9, 10], periodic contact line pinning and depinning in a circular drying geometry [32, 57], sequential dewetting of a solvent bilayer [15, 58], the formation of gas bubbles in thin solvent films [59], and magnetic interactions [54, 60]. We shall now examine some of these mechanisms in detail.

The formation of nanoparticle rings via the creation of holes in a volatile thin film has typically been thought of as a three-stage process: nucleation, growth, and arrest. Once a hole in the thin volatile film is nucleated, evaporation of solvent from the rim results in a retreat of the substrate–solvent–air contact line, i.e., the hole expands. Nanoparticles remain in solution and, thus, are collected at the rim. Eventually, growth is arrested and a nanoparticle ring is formed by deposition of the accumulated nanoparticles, see figure 6. This general theory for the self-organization of nanoparticles into rings was put forward by Ohara and Gelbart [36]. For volatile thin films, the nucleation stage can occur via two mechanisms. Holes can appear homogeneously via, for example, thermally driven nucleation, without spatial and temporal correlations of the nucleation centres (if these holes grow large enough to coalesce then cellular networks are formed). Alternatively, holes can appear heterogeneously via defect-driven nucleation, resulting in temporal correlations and, thus, rings of similar sizes. Surface defects may be topographical or chemical, or both, giving rise to wettability gradients across the substrate [61].

The Monte Carlo model described previously, and variants thereof, are capable of reproducing nanoparticle rings [13, 47]. Rings have been shown to form by allowing modification of the chemical potential to incorporate an effective thickness dependent disjoining pressure [13, 44]. Since μ incorporates both the 'true' liquid–gas chemical potential and any liquid–substrate interaction, a dynamic chemical potential allows this latter term to gain an effective thickness dependence to reflect a switch in the domination of long- to short-range forces [40] providing a route through which bimodal patterns

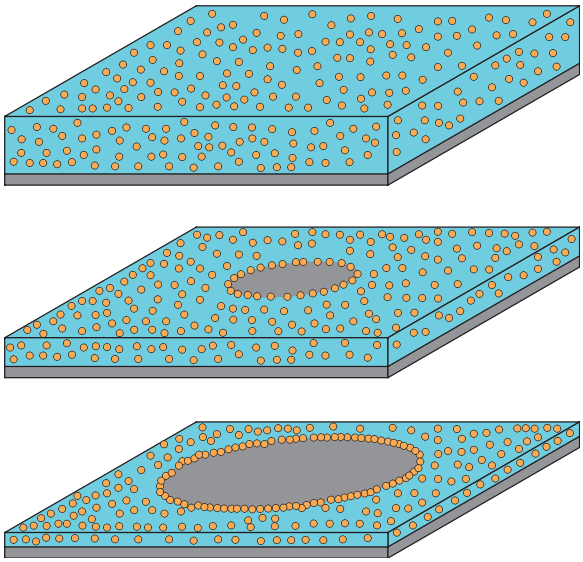

Figure 6. Illustration showing the process of nucleation and growth of a hole in a volatile wetting nanofluid film on a solid substrate. Nanoparticles are collected at the expanding rim, forming a ring when the solution dries (after Ohara and Gelbart [36]).

may form. Yosef and Rabani [47] were the first to show the formation of rings, using a fully three-dimensional Monte Carlo model. An advantage of this extension to include a film thickness is the decoupling between global solvent evaporation and evaporation of solvent from a rim. This allows a hole to expand whilst the film is thinning globally, and, once the film is very thin, global dewetting occurs to produce the surrounding smaller scale structure. An important result of this model is that it predicts that there is no upper limit of ring diameter, as its size is dictated by the thickness of the film when the nucleation event occurs—the thinner the film is when nucleated, the smaller the resultant ring. Furthermore, they found there was little dependence of ring diameter on nanoparticle concentration. This is in conflict with the continuum model developed by Ohara and Gelbart [36] which predicts an upper limit on the size of nanoparticle rings based on the concentration of nanoparticles in the precursor solution—a high concentration of nanoparticle results in small rings. Through their model the conclusion is that the growth of nanoparticle rings is arrested when the frictional force at the contact line, originating from nanoparticles–substrate interactions, overcomes expansion via evaporation at the rim.

These models of nanoparticle ring formation via the nucleation of holes, and their subsequent expansion via solvent evaporation at the rim, however successful, do not take into account the possibility of microscale water droplets condensing on either the surface of the solvent or on the substrate due to evaporative cooling. This phenomenon, known as the 'breath figure' effect, can have a major effect on the dynamics of ring formation in nanofluid systems undergoing evaporative dewetting. Evidence of this effect is shown by Khanal and Zubarev [55], where optical microscopy is used to image a dense array of small water droplets on the surface of solution of Au nanorods dispersed in dichloromethane. Following evaporation of the solvent, TEM images display a high density of nanorod rings. The small droplets of water that condense on the substrate, due to evaporative cooling, template the formation of nanorings. This highly versatile technique has been employed on a range of solutes such as nanoparticles [16], polymers [62], hybrid nanoparticle–polymer systems [63], and single-molecule magnets [64].

There also exists examples in the literature of nanoparticle rings forming through convective processes. Maillard *et al* [9, 35] showed micrometre rings of nanoparticles of various types, attributing their formation to Bénard–Marangoni convection. They concluded that by controlling the solvent evaporation rate, this convection process can be used to form isolated rings or hexagonal arrays (cellular networks). Another ring formation technique relating to convection is demonstrated by Govor *et al* [15, 58]. In these experiments, nanoparticles with an organic coating are dispersed in a mixture of hexane and water. When this solution is deposited onto the substrate, a wetting bilayer film is formed. However, due to its greater volatility, the hexane evaporates to leave nanoparticles on top of an unstable water film. This water film then decomposes into droplets. As these droplets dry, convective currents deposit nanoparticles at the edges, forming rings when evaporation of the water is complete.

Interparticle interactions can be tailored to play a key role in the formation of nanorings. Tripp *et al* [54] used 27 nm Co nanoparticles, small enough to behave as single-domain magnetic dipoles, to show a dipole-directed self-assembly route to forming nanoscale rings. The same particles are also shown to form microscale rings via evaporatively driven processes [54]. Shafi *et al* [60] discovered interesting interpenetrating nanoparticle ring structures (dubbed 'Olympic Rings') following the evaporation of a solution-containing magnetic barium hexaferrite ($BaFe_{12}O_{19}$) nanoparticles. This overlapping of nanoparticle rings cannot be explained solely by the formation of holes in an evaporating thin film; consideration of magnetic dipolar interactions is required to explain these observations.

2.4. Nanoparticle fingering

We now move on to discuss branched and fingering patterns, of which there exist countless examples in a wide variety of physical and biological systems [65], including bacterial populations [66], snow crystals [67], diffusion-limited aggregates [68], and 'viscous fingers' [69]. In this last example, branched patterns arise due to the Saffman–Taylor [70] instability at the interface of fluids with different viscosities (as can be seen in, for example, a Hele-Shaw cell), where fluctuations in a flat interface become self-amplifying. Fingering instabilities in thin nanofluid films have been documented by several research groups [9, 13, 17, 41, 47, 48, 32, 71–73], both isotropic (radial) and anisotropic (linear) fingering patterns have been observed following the dewetting of colloidal nanoparticle solutions. Isotropic branching (see figures 1(f) and 7(d)) occurs at the rims of nucleated holes in ultrathin nanofluid films, whilst anisotropic branching forms due to instabilities at the macroscopic three-phase (substrate–solution–air) contact line.

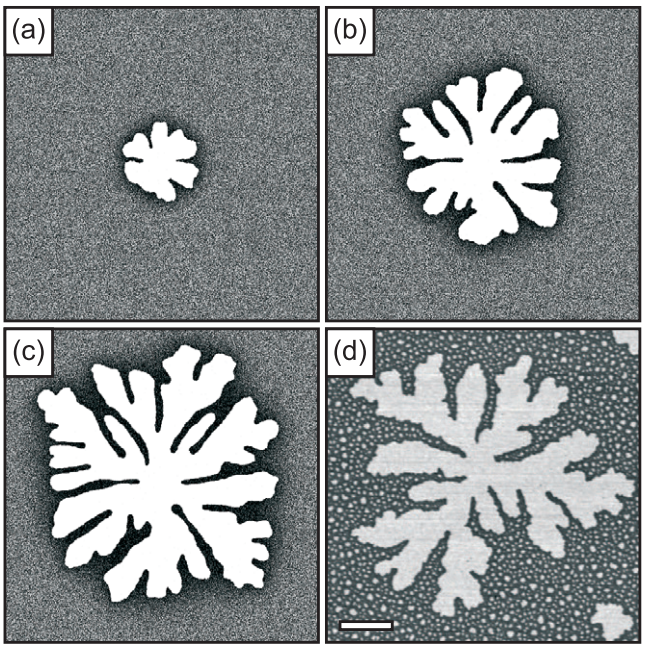

Figure 7. (a)–(c) The development of a radial fingering structure in the Monte Carlo simulation model. (Simulation parameters: $M = 4$, $\phi = 0.30$, $\mu = -2.20$, $k_B T = 0.25$.) (d) An AFM image of a microscale isotropic fingering structure. This pattern resulted from the meniscus-mediated drying of 2 nm octanethiol-passivated Au nanoparticles dispersed in chloroform on a silicon substrate. Scale bar: 1 μm.

The 3D Monte Carlo model of Yosef and Rabani [47], as previously discussed, predicted the existence of isotropic nanoparticle fingering structures. These simulations proceeded in a similar manner to those that formed nanoparticle rings, except the mobility of nanoparticles was significantly reduced. With high nanoparticle mobility, nanoparticles are able to diffuse in step with dewetting fronts to leave an impression of the solvent coverage immediately prior to complete evaporation. However, when the mobility is lowered, nanoparticles begin to accumulate at dewetting fronts. An instability develops and nanoparticles are deposited perpendicular to the retreating interface in the form of dendritic-like fingers. Figures 7(a)–(c) show an example of a fingering structure developing in the two-dimensional Monte Carlo model [13, 48].

Soon after this discovery in the numerical realm, Pauliac-Vaujour *et al* [17] documented the formation of these types of isotropic fingering patterns when using colloidal suspensions of alkanethiol-passivated 2 nm Au nanoparticles. These fingering patterns were found to develop in the ultrathin film of a colloidal solution drying in a meniscus geometry [41] (this ultrathin film remained after the macroscopic contact line passed). Large scale (elongated) anisotropic fingering patterns were also observed in these experiments, the directionality of which were imposed by the motion of the macroscopic contact line. The most likely origin was thought to be the Marangoni effect occurring at the dewetting front (Maillard *et al* [9] describe this process).

Pauliac-Vaujour *et al* found that the microscale isotropic fingering patterns could only be observed within a narrow experimental window—nanoparticle possession of low diffusivity was determined a key requisite for fingering to occur [17]. By modifying the carbon chain length of the passivating alkanethiol ligands from pentane (C_5) to tetradecane (C_{14}) they were able to control both interparticle and substrate–particle interactions. They found that fingering patterns could only observed for C_{10}, C_{12}, and C_{14} ligands. These passivating molecules are thought to provide low nanoparticle diffusivity via ligand interdigitation [74], an effect not seen for short chains [75, 76]; Pauliac-Vaujour *et al* observed the most pronounced fingering for C_{12} ligands. This was thought to be due to longer C_{14} chains possessing end gauche defects [76] which gave rise to less-pronounced interdigitation and thus a higher nanoparticle diffusivity. A second experimental variable that Pauliac-Vaujour *et al* investigated was the presence of an excess of uncoordinated alkanethiol molecules in the colloidal solution. They found that by adding an excess of just 0.1% by volume, the propensity for fingering was dramatically enhanced; the observed structures were highly ramified [17]. This was explained as being due to the excess thiol increasing the viscosity of the solution, and thus further reducing the diffusivity of nanoparticles.

These experiments revealed a set of general observations of isotropic nanoparticle fingering patterns. That is, they arise due to transverse instabilities at evaporatively dewetting fronts. The origin of the instability is the nanoparticles themselves; when the nanoparticle mobility is low, they accumulate at the front. When the local concentration of nanoparticles becomes too high, they are expelled through the instability mechanism and deposited as fingers. This effect is analogous to the auto-optimization of dewetting rates seen for some polymer films [77], where a dewetting front develops an instability which results in the deposition of droplets to avoid slowing of the front. These fingering patterns provide explicit visual evidence that nanoparticles in drying colloidal solution are not merely passive tracers. Whilst they do act as markers of the nanofluid dewetting process, they also play a role (of varying importance) in shaping the dewetting process itself.

Since these experimental observations, the fingering instability has been studied in greater detail via numerical methods. Building on the work of Yosef and Rabani [47], Vancea *et al* [48] examined the influence of many parameters in the Monte Carlo model to better understand the fingering process for linear dewetting fronts. They found that the driving force of evaporation, the chemical potential, μ, and the mobility of nanoparticles, M, strongly affected the propensity for fingering to occur; decreasing M resulted in greater fingering, decreasing μ resulted in a linear increase in front velocity which corresponded to a linear increase in the density of fingering. Interestingly, they found that the concentration of nanoparticles, ϕ, had little effect; increasing ϕ resulted in thicker fingers, but approximately the same amount. From these observations Vancea *et al* deduced that the fingering process is most closely controlled by the dynamical parameters M and μ, which determine the timescales for nanoparticle diffusion and solvent evaporation, respectively; the faster nanoparticles can diffuse away form the front, the less they will accumulate, and thus the instability is less likely to manifest.

Vancea *et al* also studied the effects of varying the nanoparticle–nanoparticle interaction strength, ϵ_n, on the fingering dewetting process [48]. They found that for low values, fingering is observed, but the pattern is nearly independent of ϵ_n indicating a purely dynamic instability. For large values, demixing of the nanoparticles and liquid prior to dewetting results in clusters of nanoparticles (no fingering). However, for intermediate values they found that the degree of fingering depends heavily on ϵ_n. They noted that nanoparticle–liquid demixing occurs at the moving front, rendering it transversally unstable, resulting in fingering patterns controlled by both the dynamics and energetics of the system. These results provide greater insight into experimental studies performed by Pauliac-Vaujour *et al* [17]. The observation of different degrees of fingering when altering the length of the passivating alkanethiol molecules may stem from variation in strength of interactions between nanoparticles, and may not be purely due to changes in the nanoparticle mobility. Longer alkanethiol molecules will result in greater nanoparticle separations and will therefore weaken van der Waals interactions between the Au cores.

One final note with respect to nanoparticle fingering: Pauliac-Vaujour *et al* [17] also looked for evidence of quantitative agreement between the morphological characteristics of experimentally observed and numerically simulated fingering patterns. This was implemented by a comparison of fractal dimensions, D_0, obtained via calculations of density–density correlation functions. They found good agreement over a decade in length scales, obtaining $\langle D_0 \rangle = 1.70(5)$ for experimental fingering, and $\langle D_0 \rangle = 1.75(5)$ for simulated fingering. It is interesting to note that these values coincide with the well-determined value of the fractal dimension for viscous fingering branched patterns ($D_0 = 1.70(2)$ [69]), suggesting some similarity in the underlying pattern formation mechanisms.

3. Controlling pattern formation

The main focus of section 2 was pattern formation in ultrathin (few nanometre thick) nanofluid films, where the resultant nanostructures are generally one nanoparticle high. This section shifts attention to methods that have been developed to tune pattern formation. Techniques to be discussed include controlling the drying geometry of a nanofluid solution, pre-patterning substrates to guide dewetting, and post-deposition manipulation of nanoparticle assemblies via local or global modification methods.

The majority of patterns discussed thus far form via spin-coating a nanofluid solution onto a solid substrate. In spin-coating, a drop of solution is placed onto a substrate which is then spun at high angular velocities, resulting in a homogeneous coverage of the substrate. Although film thinning via spin-coating is a complicated interplay of hydrodynamical and evaporative processes, it can, for simplicity, be approximately broken down into three main steps. First, as the substrate is accelerated to its final angular velocity, most of the solution is thrown off by large centrifugal forces. Once a steady angular velocity is established, viscous flow of solution towards the edge of the substrate causes the ejection of droplets which thin the solution film. Finally, when the film is sufficiently thin, solvent evaporation becomes the dominant mechanism of film thinning. This final spin-coating stage is the most important for the formation of self-organized patterns of colloidal nanoparticles. Since these nanoparticles are generally immobile on solid substrates, due to physisorption, the structures formed via spin-coating originate from dewetting patterns in the solution film prior to complete solvent evaporation. When using volatile nanofluids, the nature of solvent evaporation in spin-coating leads to nanoparticle assemblies that are considered to be far from equilibrium (and kinetically trapped there) due to rapid quenching of the system.

As mentioned in section 1, potential future applications which exploit the collective properties of nanoparticle assemblies require long-range ordered superlattices. In drying experiments, to move towards assemblies of nanoparticles considered to be close to equilibrium one would expect that the rate of solvent evaporation must be reduced. A naïve approach to slow evaporation is simply to place a droplet of solution onto a substrate and allow it to dry naturally. Depending on the nature of the substrate and solvent, a drop of solution will either wet the surface or, of concern here, form a droplet with a finite contact angle. However, the technical simplicity of this method is accompanied by complications in droplet drying dynamics.

3.1. Droplet drying

One of the most recognizable patterning features of a drying droplet containing particles is the ring stain—a deposit of particles, which were initially distributed uniformly within the droplet, concentrated along the perimeter. The phenomenon giving rise to this pattern is often referred to as the 'coffee stain' effect, as it can be clearly seen when a droplet of coffee dries to produce a ring stain (a dense accumulation of coffee particles). The origin of this patterning was explained by Deegan *et al* [78], who identified three key requirements for ring stain formation: a drop of solution on the substrate has a finite contact angle (i.e. forms a droplet); the contact line (perimeter) of the droplet is pinned at its initial position; and the solvent evaporates. Provided these conditions are met, the coffee stain effect can be observed for a range of solutes, solvents, and substrates. Self-pinning of the contact line is caused by the solute 'corrupting' the substrate [79]. Once pinned, the contact line cannot move. Subsequent evaporation removes solvent from the contact line, and a compensating flow from the centre of the droplet to the edge is established (see figure 8(a)). Solute is carried by this flow to the contact line where it accumulates in a dense ring deposit which remains once all the solvent has evaporated. If the contact line is not pinned, uniform evaporation would cause the contact line to retract and no ring stain would be observed. This insight by Deegan *et al* [78], reinforced by strong experimental evidence, showed that solute transport could originate from capillary flow, and that typical transport mechanisms such as surface tension gradients and diffusion had a negligible effect.

Deegan [79] also explored the influence of a wide range of experimental parameters on pattern formation in

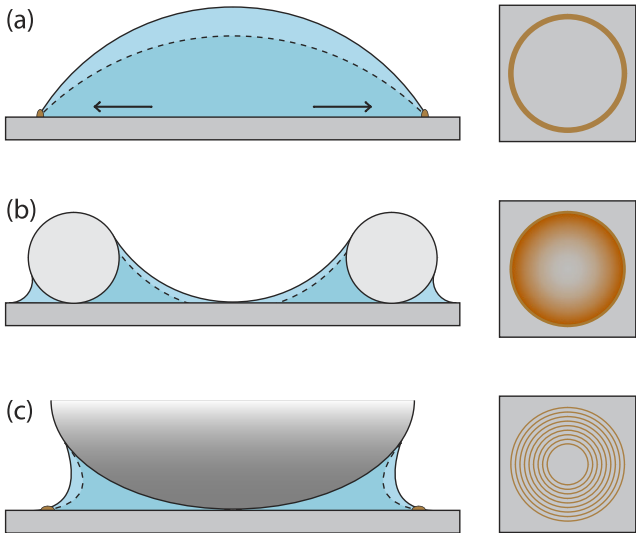

Figure 8. Illustrative diagrams displaying side views of drying nanofluid geometries and the corresponding nanoparticle assemblies viewed top-down. (a) In a solute-containing droplet, solute may pin the contact line. Flow from the centre of the droplet recompenses solvent loss via evaporation from the contact line, and carries more solute to the perimeter. After depinning, a dense 'coffee ring' stain remains (after [79]). (b) Solution adopts a meniscus geometry within a Teflon ring. Drying occurs from the centre resulting in a smooth increase in nanoparticle concentration moving out radially (after [41]). (c) A capillary bridge resulting from a sphere-on-flat geometry. Periodic pinning/depinning results in concentric rings of nanoparticles (after [32]).

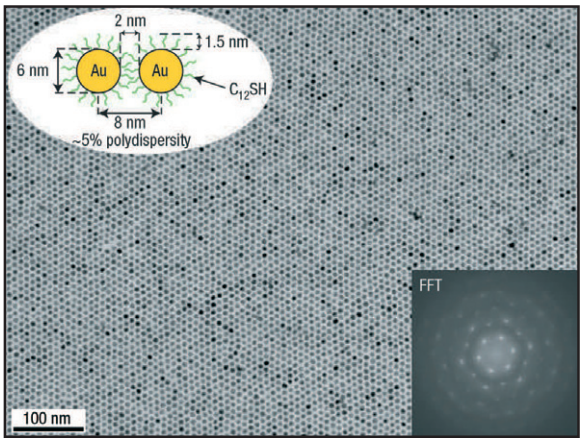

Figure 9. TEM micrograph of a long-range ordered close-packed monolayer of dodecanethiol-passivated 6 nm Au nanoparticles. The upper left inset shows ligand interdigitation of nanoparticles, the lower left inset is the fast Fourier transform of the TEM image. Reprinted by permission from Macmillan Publishers Ltd: Nature Materials, Bigioni *et al* [18], copyright 2006.

drying droplets, using an experimental system of water-dispersed sulfate-terminated microspheres on mica. Two temporal regimes of pattern formation were identified: an early stage when the self-pinning force 'exerted' by the solute is solely responsible for the contact line behaviour, and a later stage, once the contact line separates from the ring stain, where pinning forces compete with 'conventional' dewetting forces yielding patterns with evidence of wavelength selection in their wake. The resulting stains display large rings chronicling arrested contact line motion, and more complex cellular and lamellar structuring, for example, which form whilst the contact line is moving. Deegan [79] explored how the patterning can be controlled through variation of experimental parameters such as solute concentration, particle size, and surfactant concentration. This final variable, surfactant concentration, produced striking variations in the patterns observed and plays a major role in the formation of nanoparticle superlattices.

Realizing that rapid dewetting of volatile solvents can significantly undermine the degree of ordering in 2D nanoparticle superlattices, Lin *et al* modified a simple droplet drying technique to produce nanoparticle superlattices with exceptional long-range order [80]. Using solutions of 5.5 nm dodecanethiol-passivated Au nanoparticles dissolved in toluene, they also identified that dispersion of nanoparticle diameters provided another hindrance in the quest for long-range order. As such, their synthesis technique refined the well-known method reported by Brust *et al* [81] to produce highly monodisperse solutions [82]. Simply placing a drop of their solution onto a substrate and allowing it to dry in air produced disordered island and labyrinthine patterns depending on particle concentration. Beyond a given point, further increasing the concentration of nanoparticles in solution produced bilayers rather than improving the monolayer coverage/ordering. Knowing that the morphology of domain structures in their nanoparticle arrays were determined by competition between 'destructive' solvent dewetting and 'constructive' two-dimensional superlattice formation, Lin *et al* developed a technique with the intention of maintaining a wetting layer on the substrate surface such that nanoparticles have more time to self-assemble and find equilibrium positions. Once formed, this superstructure must be robust enough such that it is not perturbed when dewetting finally occurs (despite the attractive interparticle van der Waals forces being the inducing source of self-assembly to form superlattices [83], it has been shown that ligand interdigitation provides the main, surprisingly high, structural stability of two-dimensional nanoparticle superlattices [84]). Lin *et al* found that by adding a small excess of the associated low-volatility ligand molecule (dodecanethiol) to their solution, evaporation of the droplet was slowed (without introducing additional impurity species) permitting the formation of nanoparticle superlattices ordered over several microns in range. At the time this was a vast improvement over typical domains sizes of less than a few hundred nanometres reported by other research groups.

Subsequently, the formation of two-dimensional superlattices in this experimental system was studied in real time by Narayanan *et al* [85] using small angle x-ray scattering (SAXS) and by Bigioni *et al* [18] using optical microscopy; figure 9 shows a close-packed nanoparticle monolayer prepared by Bigioni *et al* [18]. A key finding of these studies was that the superlattices in this case form at the liquid–air interface. The SAXS experiments showed that when a drop of solution

is placed onto the substrate, initially there is no visible scattering pattern, indicating no ordered superstructures within the droplet. However, over time, as solvent evaporates, the intensity of scattering corresponding to in-plane long-range order increases dramatically. This scattering pattern remains fixed for hours whilst there still exists a thin liquid film (with a high dodecanethiol concentration) on the substrate. The optical microscopy studies show clear evidence of monolayer islands of Au nanoparticles on top of the solution droplet [18]. These islands subsequently merge together to form a continuous monolayer, which, after the contact line depins and the solvent recedes towards the centre, is deposited intact on the substrate. The formation of these two-dimensional superlattices was thus explained using a kinetic interface-crushing model. By calculating the diffusion constant of the nanoparticles, the random walk diffusion distance for a set time can be compared to the rate at which the liquid–air interface recedes. Narayanan *et al* [85] and Bigioni *et al* [18] both showed that the interface velocity is fast compared to nanoparticle diffusion, thus one can expect a flux of nanoparticles impinging on the liquid–air interface from below. The SAXS experiments showed that the subsequent formation of monolayer nanoparticle islands display exponential growth kinetics. This is further support for the interface-crushing model as exponential behaviour is expected if domain growth is due to the incorporation of nanoparticles impinging on the domain from below such that the rate of increase in domain size is proportional to the current domain size (domain growth via diffusion and assimilation of particles at the interface would result in power-law growth). Bigioni *et al* found that if evaporation was slowed significantly, or if solutions contained very little uncoordinated dodecanethiol, then no superlattices were observed [18]. This showed that the role of excess surfactant molecules in superlattice formation in these experiments is not to slow evaporation, but to provide an attraction to localize nanoparticles at the liquid–air interface. This rapid-evaporation technique challenges our notions of self-assembly—the process is clearly far from equilibrium, yet produces structures with exceptional long-range order and correlations at the scale of individual particles.

One final note on droplet drying concerns the self-assembly of nanorods. The formation of ordered nanorod arrays are complicated by their shape anisotropy resulting in different types of orientated assemblies. One commonly employed tactic is to apply an external electric field whilst the nanorod-containing solution is drying to control their alignment, the applied field can be static [20] or alternating [86] (the latter results in alignment due to dielectrophoretic forces). However, of interest here is the work of Nobile *et al* [87] who reported on how coffee stain evaporation dynamics affect the orientation and level of ordering in assemblies of CdSe/CdS core–shell nanorods dispersed in toluene. In simple drop drying experiments they observed ribbon-like nanorod assemblies within the dense ring stain accumulation of particles and randomly ordered rods elsewhere for solutions with low nanorod concentrations. For solutions with a high concentration of nanorods, they found that rods align in smectic structures with their long axis parallel to the ring stain. In addition to this, Nobile *et al* positioned two electrical micromanipulators within a drying droplet and applied an external electrical dipole field to stimulate circular fluid retraction. This resulted in the smectic domains arranging in stripes within the ring stain fringes.

3.2. Confined drying geometries

An interesting question arises when we consider how the overall geometry of a nanofluid film affects the dewetting dynamics which control the contact line motion and subsequent pattern formation processes. Pauliac-Vaujour and Moriarty [41] developed a technique to study the drying of an ‘inverse’ droplet—a meniscus—of a nanofluid solution. To establish this geometry, a drop of solution (alkanethiol-passivated 2 nm Au nanoparticles dispersed in toluene) was deposited within a PTFE (Teflon) ring placed on an oxide-terminated silicon substrate. Since the solution preferentially wets Teflon (compared to the substrate) a meniscus geometry is adopted instead of a droplet [41] (see figure 8(b)). This technique had previously been demonstrated in the context of polystyrene microsphere self-assembly [88, 89], but the physics involved in Pauliac-Vaujour and Moriarty’s experiments differ considerably due to the drastically reduced particle size.

The meniscus geometry presents a gradient in solvent thickness—thinnest in the centre and thickest towards the edge. Since the evaporation time for a film depends on its thickness, this system allows one to study how evaporation time affects pattern formation on a single sample. The centre of the film dries first, creating a circular contact line which gradually expands. The rate of contact line motion decreases with distance as the film becomes thicker and evaporation takes longer. This technique produces self-organized nanoparticle patterns with a smooth and reproducible graduation from worm-like patterns in the centre to close-packed void-free nanoparticle monolayers (superlattices) at the edge. In between these extremes, a range of cellular and branching structures can be observed [41]. However, nanoparticle superlattices are only observed when a small excess of alkanethiol molecules are added to the nanofluid solution, although unlike the previously discussed method [18, 80, 85], the interface-crushing effect is not at play here since superlattices form very close to the ring–substrate contact line where evaporation is extremely slow. Pauliac-Vaujour and Moriarty found that the motion of the contact line was significantly altered following the addition of excess alkanethiol to the solution. This manifested itself in oscillating contact lines (changes of direction) and transverse fluctuations which developed into macroscopic anisotropic fingering patterns [17]. Interestingly, although the excess alkanethiol altered the morphological characteristics of individual patterns, the overall graduation of particles on the substrate following deposition was largely unaffected.

In a similar vein to Pauliac-Vaujour and Moriarty’s work, an alternative to the drop drying method is solvent evaporation from a capillary bridge (formed via a sphere-on-flat experimental setup) [90, 32, 57, 91]. In this technique, a drop of a toluene-based solution is placed in the gap between an oxide-terminated silicon substrate and a spherical

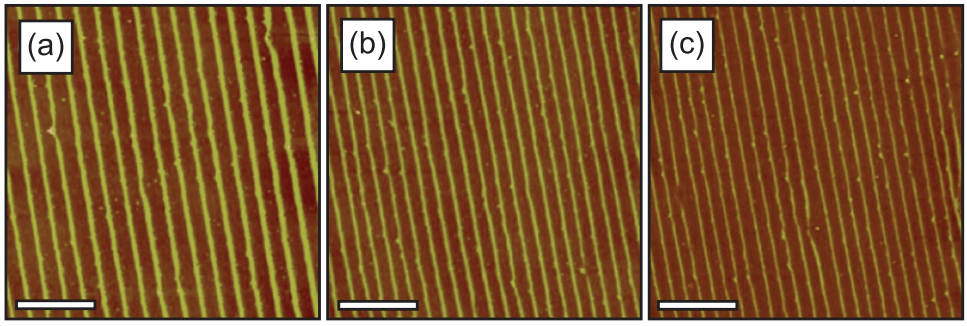

Figure 10. AFM images of γ-Fe_2O_3 nanoparticle rings (stripes when viewed locally) formed at the (a) outermost, (b) intermediate, and (c) innermost regions on the substrate. The rings are gradient concentric, closer together nearer the sphere–substrate contact point, due to nonlinear solvent loss. Scale bars: 20 μm. Reprinted by permission from the Institute of Physics Publishing, Byun *et al* [57], copyright 2009.

silica lens (inside an environmentally controlled chamber). In this confined geometry, the solution adopts a capillary-held 'meniscus' shape. The difference here is that the edge of the meniscus is exposed, thus the three-phase contact line forms at the perimeter (see figure 8(c)). Subsequent evaporation of solvent causes the contact line to retreat towards the centre, reducing its total length. The typical result of drying a nanofluid solution in this geometry is a series of concentric ring solute deposits with high regularity [90, 32, 57, 91]. These rings have been reported for both polymeric [91, 90] and nanoparticle-containing solutions [32, 57]. By characterizing these concentric rings by their height, width, and centre-to-centre separation, as a function of position on substrate, gradient rings (where characteristics depend on position) have been observed for 14 nm oleic-acid-passivated γ-Fe_2O_3 magnetic nanoparticles [57] and poly[2-methoxy-5-(2-ethylhexyloxy)-1,4-phenylenevinylene] (MEH-PPV) [90], and periodic rings (where characteristics do not depend on position) have been observed for a range of trioctylphosphine oxide (TOPO)-passivated nanoparticulates [32] and poly(ferrocenyldimethylsilane) (PFDMS) [91].

The formation of rings in this drying geometry follows from a straightforward repeated slip–stick mechanism. Evaporative loss of solvent at the perimeter results in jamming of solute to create local surface roughness which pins the contact line. Continual evaporation gradually reduces the contact angle until some critical value is reached, when the capillary (depinning) force becomes greater than the pinning force [90]. The contact line then depins, retracts (slips), and arrests (sticks) at some new position (with an increased contact angle, thus lower capillary force) leaving behind a ring of solute. This process then repeats to form a series of concentric rings of decreasing diameter. In this controlled geometry, highly regular rings are observed, unlike the typically irregular rings observed in standard drop drying experiments [79]. Xu *et al* [90, 32] found that both ring size (height and width) and centre-to-centre separation increased with increasing solute concentration (the same trend was seen with increasing solvent volatility). While increased ring size is easily rationalized, the trend in centre-to-centre separation seems less intuitive. This separation (the slip distance) is related to the volumetric loss of solvent during the previous sticking event. Greater concentrations of solute will provide a greater pinning force, thus holding the contact line in position for longer, resulting in a greater loss of solvent, and therefore a greater slip distance before re-pinning. Xu *et al* [90] explained gradient concentric rings as arising due to nonlinear solvent loss, originating from an imbalance between a linear pinning force (proportional to the length of the contact line) and a nonlinear depinning force (due to the curvature of the spherical lens) as a function of position on the substrate. Figures 10(a)–(c) show 80 μm AFM images of concentric rings (appearing locally as stripes) of γ-Fe_2O_3 nanoparticles at various positions on a substrate—towards the centre of the sample the separation between rings decreases, highlighting their gradient nature [57].

Xu *et al* also showed how this technique could produce spokes, i.e. solute deposited perpendicular to the contact line, as opposed to rings (solute deposited parallel to the contact line) by reducing the size of the nanoparticle solute [32]. They used solutions of TOPO-passivated CdSe/ZnS core-shell nanoparticles with 4.4 or 5.5 nm diameters dispersed in toluene. For 5.5 nm particles concentric rings were observed, for 4.4 nm particles spokes were exclusively observed [32]. In the latter case, the contact line was observed to move in a continuous manner developing a periodic fingering instability. Xu *et al* proposed that the smaller particle size reduces the surface roughness, thus reducing the pinning force such that a slip–stick motion is not observed and no rings are produced.

These spoke patterns are somewhat similar to those observed by Huang *et al* [71], which formed following the dewetting of a dilute Langmuir film of poly(vinyl pyrrolidone)-coated 100 nm Au nanoparticles. By performing dip-coating, providing a linear dewetting front, Huang *et al* were able to produce regular stripe patterns (10–20 μm pitch) owing to the fingering instability [71]. These patterns display excellent order/regularity, with stripe thickness and separation uniform across the entire substrate. Another linear geometry drying technique is that described by Roth *et al* [92]. In this method a drop of an aqueous solution of Ag 'nanoprisms' is placed between two surfaces of different wettability—Roth *et al* used a glass slide and a polystyrene-coated (40 nm thick) silicon substrate separated by 0.5 mm. The result of drying in this geometry is a nanoparticle film on the PS-coated Si substrate with a concentration gradient in the direction corresponding to the motion of the contact line.

3.3. Heterogeneous substrates

An alternative approach to guiding the dewetting of nanoparticle-containing solutions is to deposit onto pre-patterned heterogeneous substrates. This heterogeneity may be topographic or chemical (or both), and can be exploited to provide position dependent wetting properties. As such, when a drop of solution is placed onto a patterned substrate, selected areas will wet preferentially, and once the solvent has evaporated, the nanoparticle distribution on the surface will reflect the substrate patterning. Lenz [93] provides a succinct introduction to the wetting properties of structured surfaces. Early work by Parker *et al* [94] showed how micrometre-sized photoresist patterns on silicon substrates could influence solvent flow and the subsequent deposition locations of nanoparticles after drop deposition of 2 nm decanethiol-passivated Au nanoparticles dispersed in toluene.

Lu *et al* [95] presented a novel non-lithographic approach to directed dewetting using heterogeneous substrates. They created patterned substrates by exploiting wetting instabilities in a monomolecular layer which had been transferred to a solid substrate. Using a Langmuir–Blodgett technique, they formed lateral stripe patterns of L-α-dipalmitoyl-phosphatidylcholine (DPPC) on mica substrates. These patterns consist of 700–900 nm wide, 2 nm high stripes of DPPC separated by 150–200 nm channels of exposed mica substrate. The subsequent drop deposition of 5 nm CdSe (or CdSe/ZnS) nanoparticles dispersed in 1-phenyloctane resulted in selective deposition in the channels (on the exposed mica) following anisotropic dewetting.

Martin *et al* [44] described a lithographic technique to locally affect the self-organization of nanoparticles. They patterned hydrogen-terminated silicon substrates [H:Si(111)] with oxide regions using an AFM oxidation lithography technique. In high relative humidity environments, oxide regions form on H:Si(111) substrates when a biased metallic AFM tip is brought into close proximity to the surface (oxygen species originating from water in a capillary-held bridge between tip and surface are driven into the surface). Tip bias, relative humidity, and tip–sample separation affect the characteristics (such as width and depth) of the oxidized silicon [96]. The tip is then simply scanned across the surface in the fashion required to create the desired topographically and chemically heterogeneous substrate. When spin-coating solutions of 2 nm octanethiol-passivated Au nanoparticles dispersed in toluene, Martin *et al* observed different drying effects depending on the scale of the lithographically defined features.

For microscale oxide features (2 nm high, 4 μm side-length squares), differences in the evaporation rate were observed on and off the oxide region, see figure 11(a). Worm-like patterning was observed on the hydrogen-passivated region, and a cellular network was observed on the oxide region—a transition from spinodal-like to nucleation-and-growth-like evaporatively driven dewetting, with slower evaporation occurring on the oxide region. This apparent stronger affinity of an apolar solvent for the oxide region was rationalized by Martin *et al* in terms of greater roughness/porosity of the lithographically defined oxide as compared to the chemically etched H:Si(111). For nanoscale (<200 nm) oxide features, rupturing of the nanoparticle–solvent film was observed, creating a local flow of solvent away from oxide patterns, resulting in areas denuded of nanoparticles. The rupturing of liquid films by chemically heterogeneous substrates is known to occur due to wettability gradients [61], that is, at the transition between patterned and unpatterned regions here.

Martin *et al* also explored the effect of these oxide-patterned hydrogen-terminated surfaces when the nanoparticle-containing solution dries slowly via simple drop deposition. They observed nanoparticles preferentially adsorbing onto the oxide regions, densely covering the patterned features. This is explained as being due to the reduced mobility of nanoparticles on the oxide regions, again due to its rougher nature, such that

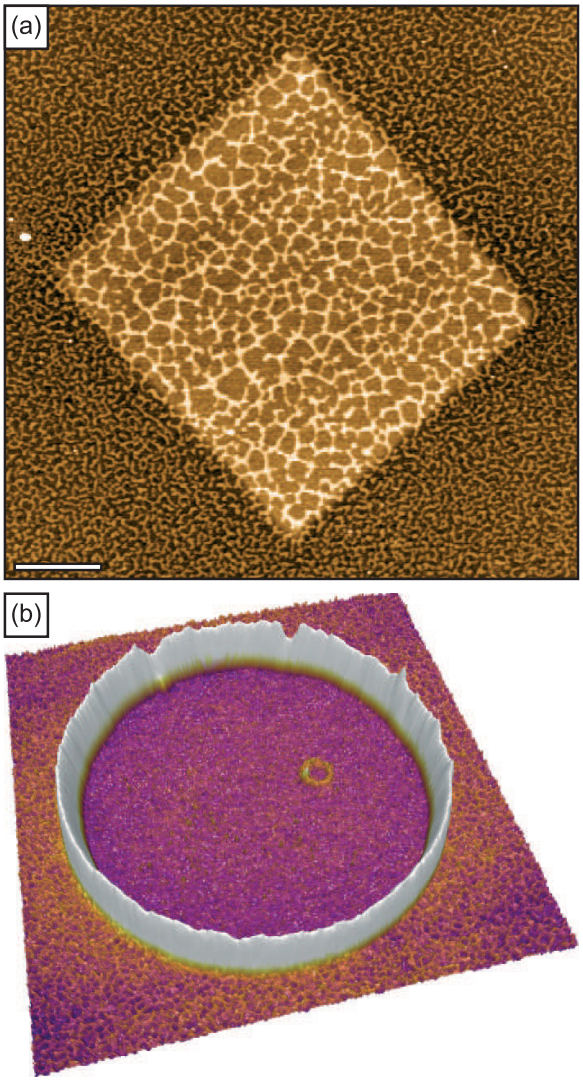

Figure 11. (a) An AFM image of Au nanoparticles spin-coated from toluene onto a H:Si(111) surface patterned with an oxide square. Scale bar: 1 μm. Martin *et al* [44], copyright American Physical Society 2007. (b) Three-dimensional rendering of an AFM image of a microscale nanoparticle ring (1.9 μm diameter, 100 nm width, 20 nm height), the formation of which was nucleated by the nanoscale lithographically defined oxide ring (150 nm diameter, 40 nm width, 2 nm height).

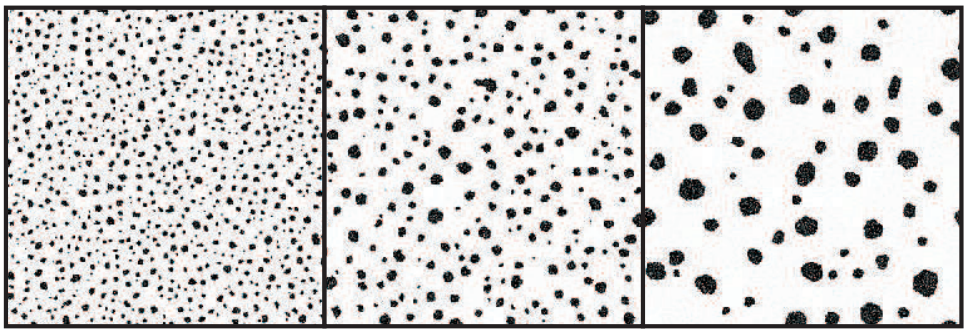

Figure 12. A series of lattice snapshots taken at equal intervals in logarithmic time, displaying simulated thermal coarsening of nanoparticle island domains (10% surface coverage). An increase in the average domain size follows from island diffusion and coalescence. (Simulation parameters: $k_BT = 1$, $\mu = -2.25$, $M = 30$, $L = 1024$.)

nanoparticles become trapped at these features as the solution dries [44].

Stannard *et al* [16] subsequently studied the formation of nanoparticle rings nucleated by lithographically defined surface oxide structures. It was observed that when using a more volatile solvent base, dichloromethane, rupturing of the nanoparticle-containing film occurred much more readily. As such, nanoparticle rings were observed to form with quasi-2D, -1D, and -0D oxide patterns (see figure 11(b) for an example). Stannard *et al* alluded to the key role of ambient water vapour in the formation of nanoparticle rings, concluding that breath figure dynamics (see section 2.3) are harnessed when solvent volatility and/or relative humidity are high, with the heterogeneous patterning acting as adsorption sites for condensing water droplets. In a similar vein, Zhang *et al* [56] have generated arrays of nanoparticle rings with diameters ranging from 3 to 26 μm using substrates, patterned via microcontact printing, with microscale checkerboard structures comprising hydrophobic and hydrophilic regions. Prior to nanoparticle deposition, water droplets condense on the hydrophilic regions. Once the solution of TOPO-capped CdSe nanoparticles dispersed in chloroform is dropped onto the substrate, water droplets act as templates for ring formation. The result is an array of nanoparticle rings with tremendous ordering/regularity over large areas.

3.4. Post-deposition pattern evolution

We now discuss a selection of routes towards evolving nanoparticle assembly patterns beyond that defined by their deposition from solution. These techniques either induce morphological changes globally, as in the case of thermal annealing [7, 25, 97], or locally, as in the case of AFM-tip-driven manipulation [8].

The model of Rabani *et al* [7], as discussed in section 2.2, is not just capable of reproducing the spatial patterns of nonequilibrium nanoparticle assemblies with high accuracy, but also displays temporal behaviour in accordance with that observed experimentally. This comparison between simulation and experiment was achieved by studying the post-dewetting thermal coarsening of nanoparticle island domains. In this system, as time progresses, there is a clear thermodynamic progression (of increased island sizes) towards a stable equilibrium. The process of coarsening concerns the evolution of domains with an increasing characteristic length scale, $L(t)$. The development of ever-larger domains proceeds in a self-similar manner and, as such, the time evolution can be described by a dynamical power law, $L(t) \sim t^{\gamma}$, where γ, the coarsening exponent, is determined by the physical constraints and dynamical nature of the system in question. In the Monte Carlo model, evolution of self-organized nanoparticle assemblies beyond the evaporation-induced structure is only possible if a thermally stable wetting layer exists at the periphery of nanoparticle domains allowing them to be fluxional [7]. Figure 12 shows an example of simulated thermal coarsening of nanoparticle islands.

In the experimental case, Rabani *et al* showed the time evolution of islands of PbSe nanoparticles spin-cast from octane (a low-volatility solvent) onto HOPG [7]. They found that this system thermally coarsens at room temperature with an exponent of $\gamma = 0.27$ (using the average domain size for $L(t)$). A similar analysis of simulations reproducing island domain coarsening gave $\gamma = 0.28$, in good agreement with experiment. Rabani *et al* further analysed the simulation data by plotting the distribution of domain sizes (scaled by $L(t)$), a more sensitive metric, which gives a time-invariant self-similar functional form. This form shows good agreement to that predicted by cluster diffusion theory where cluster diffusivity is inversely proportional to cluster size [49]. This theory also predicts a coarsening exponent of $\gamma = 1/4$. In light of these corroborating findings, Rabani *et al* concluded that thermal coarsening of nanoparticle domains proceeds via the diffusion and coalescence of domains [7].

An alternative to global thermal coarsening of nonequilibrium nanoparticle assemblies was demonstrated by Blunt *et al* [8], where an AFM operating in tapping mode was used to mechanically drive local coarsening of colloidal Au nanoparticle morphologies on silicon substrates, coercing them towards an equilibrium configuration. Despite tip–particle interactions inducing this coarsening, and the anisotropic nature of the raster scanning process, assemblies coarsened isotropically and remained two-dimensional (one nanoparticle high) throughout. Dynamic scaling was again observed, confirmed by the collapse of structure functions onto a single time-invariant master curve. Interestingly, Blunt *et al* observed

the coarsening exponent to exhibit a strong dependence on the initial pattern morphology—isolated island and interconnected labyrinthine patterns displayed significantly different values of γ.

For interconnected labyrinthine morphologies $\gamma = 0.25$ was observed using the peak wavevector of a radially averaged 2D Fourier transform as a characteristic inverse length scale. An exponent of $\gamma = 1/4$ can be attributed to Ostwald ripening of a 'spinodal' structure mediated by mass transport along domain boundaries [98]. Ostwald ripening concerns the net transfer of monomer units from small to large domains. For island morphologies, an exponent of $\gamma = 0.49$ was observed at late times following an initial low-γ transient period where the nanoparticle packing density increases without morphology coarsening. An exponent of $\gamma = 1/2$ can be attributed to Ostwald ripening with the rate-limiting process being the detachment/attachment of a nanoparticle from/to an island [99]. Sequential AFM scans by Blunt *et al* build the case for Ostwald ripening as no cluster diffusion is observed, small islands shrink until they disappear, and overall there is mass conservation of the nanoparticle assembly. However, probing the scaled island size distribution reveals a strong disagreement between these experiments and the classical mean-field form of Ostwald ripening theory. This inconsistency can be resolved by a model of Ostwald ripening which also includes binary coalescence events, as developed by Conti *et al* [100]. Since the experimental system has a large areal coverage of nanoparticles, the coalescence of growing domains is a common occurrence (as is seen in consecutive AFM scans), and mean-field approximations (such as Wagner's [99]) do not apply. Overall, the mechanical coarsening approach demonstrated by Blunt *et al* is consistent with models of modified Ostwald ripening processes for both labyrinthine and island morphologies [8].

Finally, the effects of thermal annealing at elevated temperatures have been investigated from the perspective of both two- [97] and three-dimensional 'equilibrium' close-packed nanoparticle superlattices. Both reversible melting and recrystallization [101] and irreversible disordering [24] have been observed for 3D assemblies. Robel *et al* performed a thorough analysis of the thermal stability of 2D dodecanethiol-ligated gold nanoparticle superlattices [25]. This was achieved via GISAXS in air and vacuum whilst samples were annealed at temperatures of up to 160 °C. It was found that for small elevated temperatures (<70 °C), annealing in air led to no noticeable change, whilst in vacuum a decrease in lattice constant and a loss of long-range order was observed. At greater elevated temperatures (>100 °C) ligand desorption, which leads to local sintering of nanoparticles, was observed. This effect is more pronounced in vacuum due to the increased desorption rate under low pressure.

4. Conclusions

The dewetting mechanisms which give rise to self-organized nanoparticle patterns following the deposition of nanofluids onto solid substrates have been reviewed. Relatively simple patterns such as labyrinthine structures and cellular networks were discussed first, and the various explanations which have been put forward to account for how these structures may arise were described. These included the hydrodynamic phenomenon of Bénard–Marangoni convection and evaporatively driven processes such as the nucleation and growth of holes in an ultrathin volatile film. This led into the discussion of a Monte Carlo model which is capable of reproducing a wide range of nonequilibrium nanoparticle morphologies simply from a consideration of coupled nanoparticle diffusion and solvent evaporation. Nanoparticle ring structures, of which there exist many dewetting-based formation mechanisms, were also discussed. This documentation of two-dimensional pattern types was concluded with fingering structures, the formation of which are dictated by transverse instabilities which develop at dewetting fronts. Many of the dewetting mechanisms mentioned here apply not only to nanoparticle-containing solutions, but to a wide range of solutes dispersed in volatile solvents (collagen in water [40], for example), and non-volatile dewetting systems such as polymer films [3, 4]. The resultant patterns that form can also be seen in a wide range of physical and biological systems—they are universal patterns.

A range of techniques designed to control the dewetting of nanofluids on solid substrates to produce nanoparticle assemblies with desired characteristics were discussed next. The drying of nanofluid droplets containing additional uncoordinated ligand molecules has been shown to be a simple and reliable method for producing close-packed two-dimensional nanoparticle arrays with tremendous long-range order. Evaporation of nanoparticle-containing solutions from confined geometries provides an alternative approach to controlling the characteristics of nanoparticle assemblies. Evaporation from a meniscus formed within a wettable Teflon ring produces gradient nanoparticle coverages with radial symmetry. Evaporation from a capillary bridge formed by a sphere-on-flat geometry produces concentric ring deposits which are either gradient or periodic in nature. The deposition of nanofluids onto heterogeneous substrates was examined, primarily focusing on how the rupturing of thin nanofluid films can be guided by wettability gradients. Finally, a selection of methods of global or local evolution of patterns beyond those defined by dewetting were briefly discussed.

Research into the formation of nanoparticle assemblies as mediated by the dynamics of dewetting is a burgeoning subfield of 21st century nanoscience research. This review has documented many of a terrific number of advances made in recent years. One particular expanding area of experimental research concerns the effects of ambient water vapour, both in influencing the evaporative dewetting process [16] and the subsequent evolution of self-organized morphologies. (John *et al* [102] have very recently shown a previously undocumented formation mechanism of hydrophobic nanoparticle networks on mica substrates—the nucleation and growth of water islands, as opposed to holes.) The long term stability of nanoparticle superstructures exposed to ambient conditions is a major concern for the reliability of any potential future devices and applications which exploit their collective properties, and is an issue which will most certainly be addressed in the coming years.

Acknowledgments

I would like to extend my most sincere thanks to Philip Moriarty, Matthew Blunt, Emmanuelle Pauliac-Vaujour, Christopher Martin, Uwe Thiele, and all others that I have the pleasure of collaborating with in this field of research. The writing of this article was supported by the United Kingdom Engineering and Physical Sciences Research Council (EPSRC) [EP/P502632/1] and the Leverhulme Trust [ECF/2010/0380].

References

[1] Cross M C and Hohenberg P C 1993 *Rev. Mod. Phys.* **65** 851–1112
[2] Ball P 1999 *The Self-Made Tapestry* (New York: Oxford University Press)
[3] Reiter G 1992 *Phys. Rev. Lett.* **68** 75–8
[4] Müller-Buschbaum P 2003 *J. Phys.: Condens. Matter* **15** R1549–82
[5] Seemann R, Herminghaus S and Jacobs K 2001 *J. Phys.: Condens. Matter* **13** 4925–38
[6] Ge G and Brus L 2000 *J. Phys. Chem.* B **104** 9573–5
[7] Rabani E, Reichman D R, Geissler P L and Brus L E 2003 *Nature* **426** 271–4
[8] Blunt M O, Martin C P, Ahola-Tuomi M, Pauliac-Vaujour E, Sharp P, Nativo P, Brust M and Moriarty P J 2007 *Nat. Nanotechnol.* **2** 167–70
[9] Maillard M, Motte L and Pileni M P 2001 *Adv. Mater.* **13** 200–4
[10] Stowell C and Korgel B A 2001 *Nano Lett.* **1** 595–600
[11] Moriarty P, Taylor M D R and Brust M 2002 *Phys. Rev. Lett.* **89** 248303
[12] Martin C P, Blunt M O and Moriarty P 2004 *Nano Lett.* **4** 2389–92
[13] Stannard A, Martin C P, Pauliac-Vaujour E, Moriarty P and Thiele U 2008 *J. Phys. Chem.* C **112** 15195–203
[14] Ohara P C, Heath J R and Gelbart W M 1997 *Angew. Chem. Int. Edn Engl.* **36** 1078–80
[15] Govor L V, Reiter G, Parisi J and Bauer G H 2004 *Phys. Rev.* E **69** 061609
[16] Stannard A, Alhummiany H, Pauliac-Vaujour E, Sharp J S, Moriarty P and Thiele U 2010 *Langmuir* **26** 13892–6
[17] Pauliac-Vaujour E, Stannard A, Martin C P, Blunt M O, Notingher I, Moriarty P J, Vancea I and Thiele U 2008 *Phys. Rev. Lett.* **100** 176102
[18] Bigioni T P, Lin X M, Nguyen T T, Corwin E I, Witten T A and Jaeger H M 2006 *Nat. Mater.* **5** 265–70
[19] Andres R P, Bielefeld J D, Henderson J I, Janes D B, Kolagunta V R, Kubiak C P, Mahoney W J and Osifchin R G 1996 *Science* **273** 1690–3
[20] Carbone L *et al* 2007 *Nano Lett.* **7** 2942–50
[21] Elteto K, Lin X M and Jaeger H M 2005 *Phys. Rev.* B **71** 205412
[22] Dorogi M, Gomez J, Osifchin R, Andres R P and Reifenberger R 1995 *Phys. Rev.* B **52** 9071–7
[23] Tang J, Ge G and Brus L E 2002 *J. Phys. Chem.* B **106** 5653–8
[24] Constantinides M G, Jaeger H M, Li X, Wang J and Lin X M 2007 *Z. Kristallogr.* **222** 595–600
[25] Robel I, Lin X-M, Sprung M and Wang J 2009 *J. Phys.: Condens. Matter* **21** 264011
[26] Crocker J C 2008 *Nature* **451** 528–9
[27] Parthasarathy R, Lin X M and Jaeger H M 2001 *Phys. Rev. Lett.* **87** 186807
[28] Blunt M O, Šuvakov M, Pulizzi F, Martin C P, Pauliac-Vaujour E, Stannard A, Rushforth A W, Tadić B and Moriarty P 2007 *Nano Lett.* **7** 855–60
[29] Zabet-Khosousi A and Dhirani A A 2008 *Chem. Rev.* **108** 4072–124
[30] Šuvakov M and Tadić B 2010 *J. Phys.: Condens. Matter* **22** 163201
[31] Blunt M O, Stannard A, Pauliac-Vaujour E, Martin C P, Vancea I, Šuvakov M, Thiele U, Tadić B and Moriarty P 2010 Patterns and pathways in nanoparticle self-organisation *Oxford Handbook of Nanoscience and Technology* vol 1 *Basic Aspects* ed A V Narlikar and Y Y Fu (New York: Oxford University Press)
[32] Xu J, Xia J and Lin Z 2007 *Angew. Chem. Int. Edn* **46** 1860–3
[33] Koch S W, Desai R C and Abraham F F 1983 *Phys. Rev.* A **27** 2152–67
[34] Bénard H 1900 *Rev. Gen. Sci. Pure Appl.* **11** 1261–309
[35] Maillard M, Motte L, Ngo A T and Pileni M P 2000 *J. Phys. Chem.* B **104** 11871–7
[36] Ohara P C and Gelbart W M 1998 *Langmuir* **14** 3418–24
[37] Michielsen K and De Raedt H 2001 *Phys. Rep.* **347** 461–538
[38] Weaire D and Rivier N 1984 *Contemp. Phys.* **25** 59–99
[39] Frehill F, Schulte K H G, Martin C P, Wang L, Patel S, Purton J A, Vos J G and Moriarty P 2004 *Langmuir* **20** 6421–9
[40] Thiele U, Mertig M and Pompe W 1998 *Phys. Rev. Lett.* **80** 2869–72
[41] Pauliac-Vaujour E and Moriarty P 2007 *J. Phys. Chem.* C **111** 16255–60
[42] Sztrum C G and Rabani E 2006 *Adv. Mater.* **18** 565–71
[43] Kletenik-Edelman O, Sztrum-Vartash C G and Rabani E 2009 *J. Mater. Chem.* **19** 2872–6
[44] Martin C P, Blunt M O, Pauliac-Vaujour E, Stannard A, Moriarty P, Vancea I and Thiele U 2007 *Phys. Rev. Lett.* **99** 116103
[45] Kletenik-Edelman O, Ploshnik E, Salant A, Shenhar R, Banin U and Rabani E 2008 *J. Phys. Chem.* C **112** 4498–506
[46] Sztrum C G, Hod O and Rabani E 2005 *J. Phys. Chem.* B **109** 6741–7
[47] Yosef G and Rabani E 2006 *J. Phys. Chem.* B **110** 20965–72
[48] Vancea I, Thiele U, Pauliac-Vaujour E, Stannard A, Martin C P, Blunt M O and Moriarty P J 2008 *Phys. Rev.* E **78** 041601
[49] Ge G and Brus L E 2001 *Nano Lett.* **1** 219–22
[50] Siepmann P, Martin C P, Vancea I, Moriarty P J and Krasnogor N 2007 *Nano Lett.* **7** 1985–90
[51] Cheng G, Puntes V F and Guo T 2006 *J. Colloid Interface Sci.* **293** 430–6
[52] Zhou W L, He J, Fang J, Huynh T A, Kennedy T J, Stokes K L and O'Connor C J 2003 *J. Appl. Phys.* **93** 7340–2
[53] Jang J and Oh J H 2004 *Langmuir* **20** 8419–22
[54] Tripp S L, Pusztay S V, Ribbe A E and Wei A 2002 *J. Am. Chem. Soc.* **124** 7914–5
[55] Khanal B P and Zubarev E R 2007 *Angew. Chem. Int. Edn* **46** 2195–8
[56] Zhang L, Si H Y and Zhang H L 2008 *J. Mater. Chem.* **18** 2660–5
[57] Byun M, Wang J and Lin Z 2009 *J. Phys.: Condens. Matter* **21** 264014
[58] Govor L V, Parisi J, Bauer G H and Reiter G 2009 *J. Phys.: Condens. Matter* **21** 264015
[59] Schenning A P H J, Benneker F B G, Geurts H P M, Liu X Y and Nolte R J M 1996 *J. Am. Chem. Soc.* **118** 8549–52
[60] Shafi K V P M, Felner I, Mastai Y and Gedanken A 1999 *J. Phys. Chem.* B **103** 3358–60
[61] Konnur R, Kargupta K and Sharma A 2000 *Phys. Rev. Lett.* **84** 931–4
[62] Bunz U H F 2006 *Adv. Mater.* **18** 973–89
[63] Böker A *et al* 2004 *Nat. Mater.* **3** 302–6
[64] Gómez-Segura J, Kazakova O, Davies J, Josephs-Franks P, Veciana J and Ruiz-Molina D 2005 *Chem. Commun.* **45** 5615–7

[65] Mandelbrot B B 1983 *The Fractal Geometry of Nature* (New York: Freeman)
[66] Ball P 2009 *Branches* (New York: Oxford University Press)
[67] Libbrecht K G 2005 *Rep. Prog. Phys.* **68** 855–95
[68] Viscek T 1989 *Fractal Growth Phenomena* (Singapore: World Scientific)
[69] Praud O and Swinney H L 2005 *Phys. Rev.* E **72** 011406
[70] Saffman P G and Taylor G 1958 *Proc. R. Soc.* A **245** 312–29
[71] Huang J, Kim F, Tao A R, Connor S and Yang P 2005 *Nat. Mater.* **4** 896–900
[72] Thiele U, Vancea I, Archer A J, Robbins M J, Frastia L, Stannard A, Pauliac-Vaujour E, Martin C P, Blunt M O and Moriarty P J 2009 *J. Phys.: Condens. Matter* **21** 264016
[73] Archer A J, Robbins M J and Thiele U 2010 *Phys. Rev.* E **81** 021602
[74] Luedtke W D and Landman U 1996 *J. Phys. Chem.* **100** 13323–9
[75] Hostetler M J, Stokes J J and Murray R W 1996 *Langmuir* **12** 3604–12
[76] Motte L and Pileni M P 2000 *Appl. Surf. Sci.* **164** 60–7
[77] Reiter G and Sharma A 2001 *Phys. Rev. Lett.* **87** 166103
[78] Deegan R D, Bakajin O, Dupont T F, Huber G, Nagel S R and Witten T A 1997 *Nature* **389** 827–9
[79] Deegan R D 2000 *Phys. Rev.* E **61** 475–85
[80] Lin X M, Jaeger H M, Sorensen C M and Klabunde K J 2001 *J. Phys. Chem.* B **105** 3353–7
[81] Brust M, Walker M, Bethell D, Schiffrin D J and Whyman R 1994 *J. Chem. Soc., Chem. Commun.* 801–2
[82] Lin X M, Sorensen C M and Klabunde K J 2000 *J. Nanopart. Res.* **2** 157–64
[83] Ohara P C, Leff D V, Heath J R and Gelbart W M 1995 *Phys. Rev. Lett.* **75** 3466–9
[84] Mueggenburg K E, Lin X M, Goldsmith R H and Jaeger H M 2007 *Nat. Mater.* **6** 656–60
[85] Narayanan S, Wang J and Lin X M 2004 *Phys. Rev. Lett.* **93** 135503
[86] Harnack O, Pacholski C, Weller H, Yasuda A and Wessels J M 2003 *Nano Lett.* **3** 1097–101
[87] Nobile C, Carbone L, Fiore A, Cingolani R, Manna L and Krahne R 2009 *J. Phys.: Condens. Matter* **21** 264013
[88] Denkov N, Velev O, Kralchevski P, Ivanov I, Yoshimura H and Nagayama K 1992 *Langmuir* **8** 3183–90
[89] Gigault C, Dalnoki-Veress K and Dutcher J R 2001 *J. Colloid Interface Sci.* **243** 143–55
[90] Xu J, Xia J, Hong S W, Lin Z Q, Qiu F and Yang Y L 2006 *Phys. Rev. Lett.* **96** 066104
[91] Hong S W, Xu J, Xia J, Lin Z, Qiu F and Yang Y 2005 *Chem. Mater.* **17** 6223–6
[92] Roth S V, Kuhlmann M, Walter H, Snigirev A, Snigireva I, Lengeler B, Schroer C G, Burghammer M, Riekel C and Müller-Buschbaum P 2009 *J. Phys.: Condens. Matter* **21** 264012
[93] Lenz P 1999 *Adv. Mater.* **11** 1531–4
[94] Parker A J, Childs P A, Palmer R E and Brust M 2001 *Nanotechnology* **12** 6–10
[95] Lu N *et al* 2004 *Nano Lett.* **4** 885–8
[96] Avouris P, Hertel T and Martel R 1997 *Appl. Phys. Lett.* **71** 285–7
[97] Korgel B A 2001 *Phys. Rev. Lett.* **86** 127–30
[98] Ernst H J, Fabre F and Lapujoulade J 1992 *Phys. Rev. Lett.* **69** 458–61
[99] Wagner C 1961 *Z. Elektrochem.* **65** 581–91
[100] Conti M, Meerson B, Peleg A and Sasorov P V 2002 *Phys. Rev.* E **65** 046117
[101] Sandhyarani N, Antony M P, Selvam G P and Pradeep T 2000 *J. Chem. Phys.* **113** 9794–803
[102] John N S, Raina G, Sharma A and Kulkarni G U 2010 *J. Chem. Phys.* **133** 094704